Development of a Low-Cost Interrogation System Applied to Fiber Optic Based Devices for Sensing

João Carlos Costa Araújo
Mestrado em Engenharia Física
Departamento de Física e Astronomia
2022

Orientador
Dr. Luís Coelho, Investigador, INESC TEC

Coorientador
Prof. José Almeida, Investigador, INESC TEC / UTAD

U.PORTO

FACULDADE DE CIÊNCIAS
UNIVERSIDADE DO PORTO

Todas as correções determinadas pelo júri, e só essas, foram efetuadas.

O Presidente do Júri,

Porto, _____/_____/_____

Sworn Statement

I, João Araújo, enrolled in the Master Degree of Engineering Physics at the Faculty of Sciences of the University of Porto hereby declare, in accordance with the provisions of paragraph a) of Article 14 of the Code of Ethical Conduct of the University of Porto, that the content of this dissertation reflects perspectives, research work and my own interpretations at the time of its submission.

By submitting this dissertation, I also declare that it contains the results of my own research work and contributions that have not been previously submitted to this or any other institution.

I further declare that all references to other authors fully comply with the rules of attribution and are referenced in the text by citation and identified in the bibliographic references section. This dissertation does not include any content whose reproduction is protected by copyright laws.

I am aware that the practice of plagiarism and self-plagiarism constitute a form of academic offense.

João Araújo

September 30, 2022

UNIVERSIDADE DO PORTO

MASTERS THESIS

Development of a Low-Cost Interrogation System Applied to Fiber Optic Based Devices for Sensing

Author:
João Araújo

Supervisor:
Luís Coelho

Co-supervisor:
Prof. José Almeida

A thesis submitted in fulfilment of the requirements
for the degree of MSc. Engineering Physics

at the

Faculdade de Ciências da Universidade do Porto
Departamento de Física e Astronomia

September 30, 2022

" Every passing hour brings the Solar System forty three thousand miles closer to Globular Cluster M13 in Hercules — and still there are some misfits who insist that there is no such thing as progress. "

Kurt Vonnegut Jr., The Sirens of Titan

Acknowledgements

I would like to express my deepest gratitude to my supervisors Dr. Luís Coelho and Dr. José de Almeida for the guidance, encouragement, and feedback they have given me throughout the writing of this Master Thesis. Without their advice and criticism this work wouldn't exist.

I would also like to thank all my colleagues at INESC TEC, namely, Paulo Santos for all the support, assistance, and inspiration he gave me in every step of this journey, Bernardo Dias for collaborating and helping me in every way he could and João Mendes for teaching me the most basic things and tolerating me at his lab.

I must also thank all my friends for their companionship and support, without which I wouldn't have been able to complete this work. Specifically, I must thank Bernardo Campilho, João Relvas, João Silva and Rodrigo Silva, whose mere presence these last five years has helped me overcome very difficult times.

Finally, I would like to acknowledge my family. My parents Olinda and João, for making me the person I am today and supporting my choices, and my sister Cândida, for tolerating my nonsense and for all the care she has shown me.

UNIVERSIDADE DO PORTO

Abstract

Faculdade de Ciências da Universidade do Porto
Departamento de Física e Astronomia

MSc. Engineering Physics

Development of a Low-Cost Interrogation System Applied to Fiber Optic Based Devices for Sensing

by João Araújo

The interrogation of fiber optic sensors often relies on complex and costly devices with low portability due to their size. Long Period Fiber Gratings (LPFGs) are structures with spectral behavior that presents well defined rejection bands whose spectral position is dependent on external parameters, allowing them to be used as sensors. Even though they can be formed in common and cheap telecommunication fiber, the typical interrogation methods involve the use of Optical Spectrum Analyzers (OSA) which are expensive and only suited to laboratory tests, or dedicated commercial Braggmeters with limited spectral response ranges.

With the advancement of micro-spectrometer technologies, devices such as Micro-Electromechanical Systems (MEMS) with Fabry-Pérot tunable filters are being studied as possible alternatives.

In this work, an interrogation unit was designed and built using a MEMS Fabry-Pérot Interferometer (MEMS-FPI) spectral sensor with a spectral response in the range from 1350 to 1650nm. Deconvolution techniques were used to reduce the impact of the tunable filter's impulse response in the measured signal. The performance of the unit was validated with the interrogation of LPFGs as temperature and refractive index sensors, and preliminary results for the relative humidity monitoring were presented. For the temperature a sensitivity of $0.135 \pm 0.007 nm/^{\circ}C$ was obtained, which showed a 4.9% relative error when compared to the same measurement with a commercial OSA. For the refractive index a sensitivity of 147 ± 11 nm/RIU was obtained which showed a relative error lower than 1% when compared to the OSA. These results are comparable to those obtained with

the OSA which shows the system's potential as a cheaper and more transportable alternative.

UNIVERSIDADE DO PORTO

Resumo

Faculdade de Ciências da Universidade do Porto
Departamento de Física e Astronomia

Mestrado em Engenharia Física

Desenvolvimento de um Sistema de Interrogação de Baixo Custo Aplicado a Dispositivos Baseados em Fibra Ótica para Sensorização

por João Araújo

A interrogação de sensores de fibra ótica depende frequentemente de dispositivos complexos e de custo elevado, com baixa portabilidade devido ao seu tamanho. Redes de período longo em fibra Ótica são estruturas com comportamento espectral que apresenta bandas de rejeição bem definidas, cuja posição espectral depende de parâmetros externos, o que permite a sua utilização como sensores. Embora possam ser formadas em fibra de telecomunicações comum e de baixo custo, os métodos de interrogação mais comuns envolvem a utilização de analisadores de espectro ótico, que são dispendiosos e apenas adequados para testes de laboratório, ou "Braggmeters"comerciais dedicados com gamas de resposta espectral limitadas. Com o avanço de tecnologias de micro-espectrometria, dispositivos como sistemas electromecânicos com filtros sintonizáveis Fabry-Pérot estão a ser estudados como possíveis alternativas.

Neste trabalho foi desenhada e construída uma unidade de interrogação utilizando um sistema electromecânico com Interferómetro Fabry-Pérot com resposta espectral na gama de 1350 a 1650 nm. Foram utilizadas técnicas de desconvolução para reduzir o impacto da resposta impulsional do filtro sintonizável no sinal medido. O desempenho da unidade foi validado com a interrogação de redes de período longo como sensores de temperatura e índice de refração, e apresentados resultados preliminares para a monitorização de humidade relativa. Para a temperatura foi obtida uma sensibilidade de $0.135 \pm 0.007 nm/^{\circ}C$ que mostrou um erro relativo de 4,9% quando comparado com a mesma medição com um analisador de espetro ótico comercial. Para o índice de refração obteve-se uma sensibilidade de 147 ± 11nm/RIU, que mostrou um erro relativo inferior

a 1% quando comparado com o analisador de espetro ótico. Estes resultados são comparáveis aos obtidos com o analisador de espetro ótico, o que mostra o potencial do sistema como uma alternativa com um custo inferior e portátil.

Contents

List of Figures

Glossary

LPFG	Long Period Fiber Grating
FBG	Fiber Bragg Grating
RI	Refractive Index
MEMS-FPI	Micro-Electro-Mechanical System Fabry-Perot Interferometer
FWHM	Full Width at Half Maximum
BFL	Back Focal Length
NA	Numerical Aperture
PCB	Printed Circuit Board
ADC	Analog-to-Digital Converter
DAC	Digital-to-Analog Converter
PVA	Polyvinyl Alcohol
SSE	Sum of Squares Due to Error
RH	Relative Humidity

Chapter 1

Introduction

1.1 Research Goals

Optical fiber sensor interrogation often relies on complex and expensive devices with low portability due to their size, such as Optical Spectrum Analyzers (OSA) or high resolution commercial Braggmeters. Recent advances have been made in microspectrometer devices, such as Micro-Electromechanical Systems (MEMS) with Fabry-Pérot tunable filters, which are emerging as more compact and low-cost alternatives.

This work, conducted at INESC TEC's Centre of Applied Photonics, aims to develop an interrogation unit capable of near-infrared spectroscopy using a MEMS Fabry-Pérot Interferometer (MEMS-FPI) with a tunable filter with a working range of 1350 to 1650nm. This unit is designed to be cost-effective, with low-power consumption and light-weight.

Long Period Fiber Gratings (LPFGs) have been shown to have the ability to withstand a variety of harsh environments, chemicals and electromagnetic interference. They present broad rejection bands and good sensitivity in the near-infrared region and are relatively easy to manufacture. Because of this, these structures are studied and implemented as sensors to validate the developed interrogation unit, comparatively to commercial options such as OSAs.

1.2 Thesis Structure

This thesis is composed of six chapters which detail the research work involved in the design and construction of the developed interrogation unit.

Chapter 1 presents the reader with the research goals, thesis structure and related publications.

Chapter 2 shows a study of long period fiber gratings, including a brief historical introduction, working principles and state-of-the-art fabrication methods. A way to model and simulate the spectral behavior of these structures is also presented, as well as a concise overview of common interrogation techniques.

Chapter 3 starts by describing the working principles of interrogation with tunable Fabry-Pérot filters as well as showing the characteristics of the spectrum sensor used in the developed interrogation unit. A theoretical overview of Wiener Filtering is provided and a study in the optimization of light that reaches the sensor's photodetector is also shown.

Chapter 4 presents the development of the interrogation unit, including a description of the circuitry designed for the control of the filter voltage and for the amplification of the photodetector signal.

Chapter 5 shows the discussion of experimental results obtained by the interrogation unit developed. It includes the results of deconvoluted spectra and measurements of Long Period Fiber Gratings as temperature, refractive index and humidity sensors.

Chapter 6 summarizes the work presented and presents a discussion of possible future work.

1.3 Associated Research Outputs

Part of the work developed in this thesis was submitted to the 5th International Conference on Application of Optics and Photonics (AOP2022) resulting in an oral presentation on 19th of july 2022. That same research was submitted for publication in the proceedings book of the conference.

A scientific paper is also being prepared for publication in a international journal based of the research developed in this thesis.

Chapter 2

Long Period Fiber Gratings

2.1 Introduction

Over the years optical fiber-based sensors have been applied in a large number of applications and have become the subject of extensive research. Most notably, optical fiber gratings have gathered the interest of the scientific community due to their versatility, easy manufacture, and low cost [1].

Two types of optical fiber gratings can be considered, Fiber Bragg Gratings (FBG) and Long Period Fiber Gratings (LPFG). The former was first demonstrated at the Canadian Communications Research Center by Hill et al. [2] in 1978 and were obtained by periodic perturbations in the fiber's refractive index (RI). The latter was introduced in 1996 by Vengsarkar et al. [3] and differs from FBGs in the periodicity: while FBG's are usually sub-micron, LPFGs are typically manufactured with a marking periods from $100\mu m$ to $1000\mu m$ [3, 4].

In FBGs the forward-propagating core mode is coupled to the backward propagating core mode, whereas in LPFGs the forward propagating core mode is coupled to the cladding modes which propagate in the same direction [4, 5]. These phenomena depend on the local environment. This means that changes in parameters such as temperature, refractive index or strain will affect the resulting spectrum in real time, allowing for the use of the gratings as sensors [4, 5].

These gratings present several characteristics which make them capable sensors. As they are manufactured in optical fiber they possess immunity to electromagnetic interference and because of low attenuation coefficients they allow for the implementation of systems with high lengths without expressive losses. They are also better suited to certain

environments than electrical sensors, such as in contact with liquids or even in satellite applications [6]. Due to their short grating periods, FBGs usually require more complex manufacturing systems than LPFGs. LPFGs present larger spectral bands and good sensitivity in the infra-red range, making them optimal sensors to be used with the developed interrogation unit.

2.2 Working Principle of Long Period Gratings

A Long Period Fiber Grating is formed by applying a modulation in the core refractive index which allows light coupling between the core to superior order cladding modes. This means that they work as a selective filter with well-defined rejection bands at different wavelengths.

A three-layer model for the optical fiber can be considered [7], like the one in the figure 2.1. When a grating is made, new effective indexes are created which are given by $n1 < n_{eff} < n2$ in the core and $n2 < n_{eff} < n3$ in the cladding.

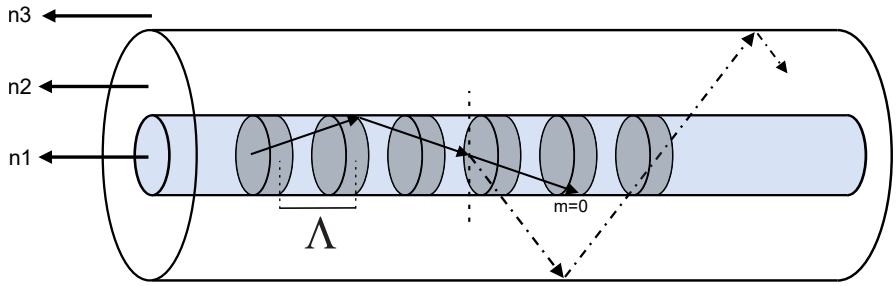

FIGURE 2.1: Coupling of the core mode to a higher order co-propagating cladding-mode induced by the long period grating. The fiber cross-section can also be seen where the refractive index of the core, cladding and external medium are represented by $n1$,$n2$ and $n3$, respectively. Adapted from Erdogan [7].

Because the LPFG acts as a diffraction grating, we can express its effect using the grating equation [8, 9]:

$$n \sin\theta_2 = n \sin\theta_1 + m\frac{\lambda}{\Lambda} \tag{2.1}$$

where Λ is the spatial periodicity between the markings in the fiber, θ_2 is the angle of the diffracted wave and m is the diffraction order. In the case of a fiber grating, this is dominated by the first order which means $m = -1$ [8].

In a single-mode fiber the propagation constant can be given by:

$$\beta = \frac{2\pi}{\lambda} n_{eff} \tag{2.2}$$

which means that the grating equation can be rewritten as:

$$\beta_{co} - \beta_{cl}^{(n)} = \frac{2\pi}{\Lambda} \tag{2.3}$$

where β_{co} is the propagation constant in the core mode, and $\beta_{cl}^{(n)}$ is the propagation constant in the cladding mode of order n. In the case of LPFGs both the core and cladding modes travel in the same direction and there is no reflection, which means all propagation constants are positive [8].

These conditions create discrete resonance wavelengths which satisfy the resonance condition:

$$\lambda_{res} = (n_{eff}^{co} - n_{eff}^{cl,n})\Lambda \tag{2.4}$$

Figure 2.1 illustrates the coupling of the core mode to the co-propagating cladding modes which happens when equation 2.4 is satisfied. At these wavelengths light is effectively filtered causing the appearance of the characteristic attenuation bands.

An example of the transmission spectrum of an LPFG can be seen in figure 2.2. It can be seen that higher order cladding modes suffer higher attenuation which explains the deeper bands at higher wavelengths.

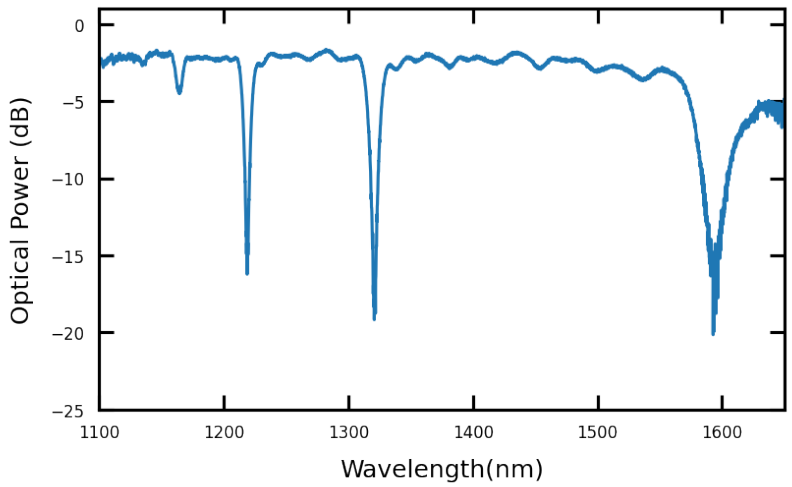

FIGURE 2.2: Transmission spectrum of an LPFG manufactured in SMF-28 fiber using the electric arc method.

2.3 Fabrication Methods

As was already mentioned, the LPFG relies on a periodic perturbation of the optical properties of the fiber. This can be achieved by applying a periodic modulation on the core refractive index or by physical deformations of the fiber itself. These perturbations are what allow the coupling to the co-propagating cladding modes.

2.3.1 UV Light Exposure Fabrication

UV light exposure is one of the most used methods for fabricating LPFGs. This is, in part, due to the fact that a lot of FBG fabrication setups that were already in place could be easily adapted to produce LPFGs instead [4, 10]. Wavelengths between approximately 193 and 266 nm are used to create the RI modulation [4, 11]. This modulation is related to the formation of glass defects associated with the Germanium present in the doping of the fiber's core [4].

Originally, UV light methods involved the use of a phase-mask placed in proximity of the fiber which allowed its marking. This mask has a diffraction array that causes an interference pattern to form at the fiber's core. This is represented in figure 2.3 (a). However, this method presents some disadvantages such as a higher cost of the setup and availability of masks which limits the possible grating periods.

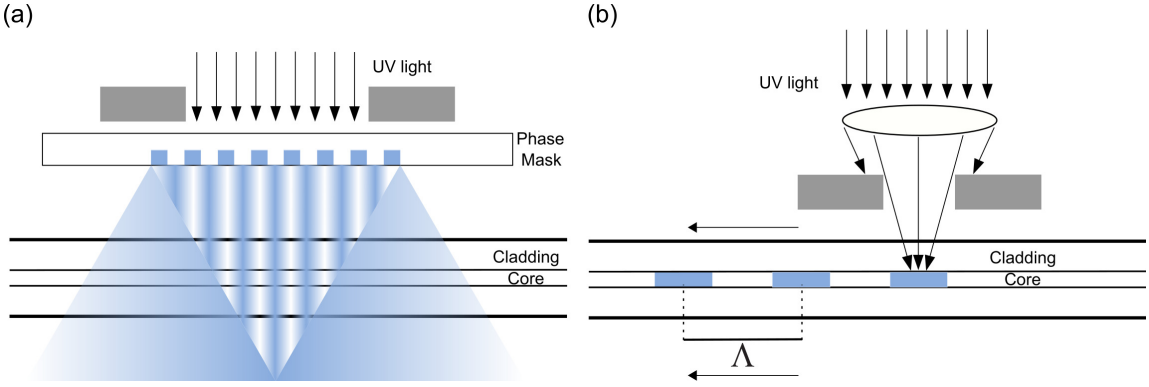

FIGURE 2.3: LPFG fabrication using UV marking techniques:(a) phase-mask method and (b) step-by-step method (image adapted from Martinez-Rios et al. [12])

With the widespread appearance of computerized translation stages a "step by step" approach became increasingly popular, in which each point is marked individually. This method is illustrated in figure 2.3 (b). After the formation of each grating groove the fiber is displaced by a distance equal to the desired grating period and the procedure is repeated [11]. This can be done using, for example, a laser beam followed by a lens and

including a mask with a single slit, through which the UV light is focused [10, 11]. This means that this approach has great versatility and allows for the fabrication of gratings of different periods in the same setup without the need of a specific mask.

2.3.2 Electric-arc Induced Fabrication

This method was first demonstrated by Poole et al. [13]. It consists in the application of electric-arc discharges in the fiber, followed by a displacement equal to the desired grating period. Each point is marked individually, making this a "step by step" method. The fiber is aligned between two electrodes and fixed to a translation stage [9]. An electrode setup can be seen in figure 2.4.

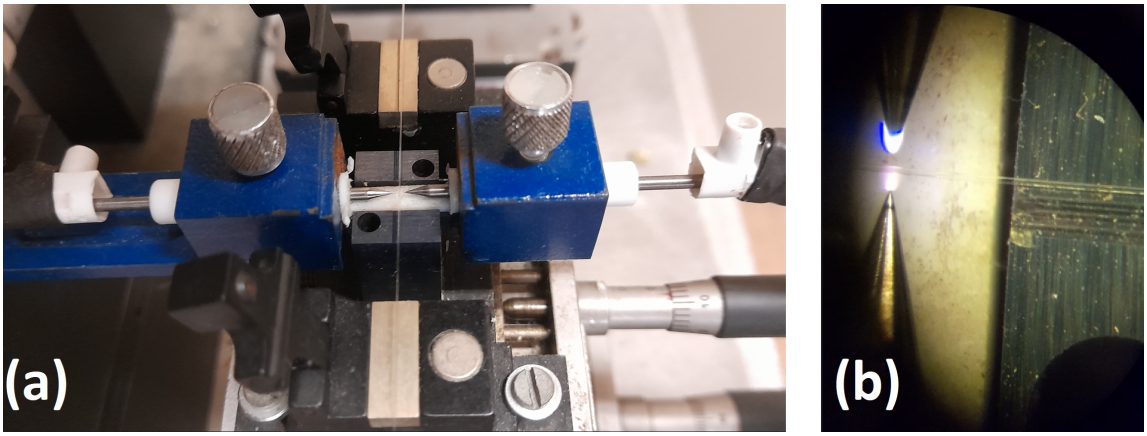

FIGURE 2.4: Electrodes used in electric-arc induced fabrication. (a) shows a photograph of the stage and micrometric screws that align the electrodes. (b) shows a photograph the microscope view of the electrodes during a discharge.

There are several advantages to this approach. Firstly, the setup is relatively simple compared to, for example, the UV radiation techniques. It also doesn't require expensive devices, making it more cost efficient. It can mark LPFGs in all kinds of fibers, including those that are non-photosensitive, meaning it doesn't require exposure to H_2 gas or post fabrication annealing [9, 14].

Additionally, LPFGs fabricated by this method have better thermal stability given that their formation mechanisms originate on thermal effects. Because of this, they are usually considered good high-temperature sensors. It has been shown that these gratings can resist temperatures of about 1000ºC without degradation of their spectra [15].

2.3.3 Other Fabrication Methods

Infrared femtosecond lasers have also been used for the fabrication LPFGs using "step-by-step" approaches [16, 17]. The RI is changed by a densification of the glass [4] and this method doesn't require the fiber to be photo-sensitive and requires no phase-mask. Most of the complications of this technique come from the alignment of the fiber core and the focus of the beam [18].

Carbon dioxide lasers (CO_2) can be used in a similar fashion [19], causing a RI change as a result of breakage of Si-O-Ge chains and a heating effect like in the electric arc technique [20].

Another method involves the geometric modulation of the fiber diameter resulting in a corrugated structure. This can be done mechanically [21] or by chemical etching [22].

2.4 Fabrication Setup

The gratings used in the work of this thesis were made using the electric arc method described in 2.3.2. The setup is shown in figure 2.5.

The fiber is secured in a linear stage commanded by a microcontroller (model IT6D CA2) with a precision of $0.1\mu m$. At the electrodes, the fiber's position can be adjusted with the use of micrometric screws. It is important that the fiber be positioned in the center, at the height of the electrodes. To help with the placement, a microscope is mounted above. The fiber end is clamped with small magnets that add enough weight to have the fiber in a tension state. The electrodes are made of tungsten doped with thorium and need to be replaced after long periods of use due to exposure to silica particles and oxidation. Worn electrodes can be polished to be used again. Usually, when fabricating, the fiber is connected to an Optical Spectrum Analyzer (OSA) so that the LPFG spectrum can be seen as the discharges are made.

The setup is connected to a computer with a LABVIEW program that allows for the automation of the fabrication process. The interface allows for the specification of the number of discharges and the grating period, which is the displacement length of the fiber suffers between discharges.

The optical fiber used is common single-mode telecommunication fiber, Corning SMF-28. This fiber presents a cladding diameter of $125\mu m$ and a core diameter of $8.2\mu m$. This

(a)

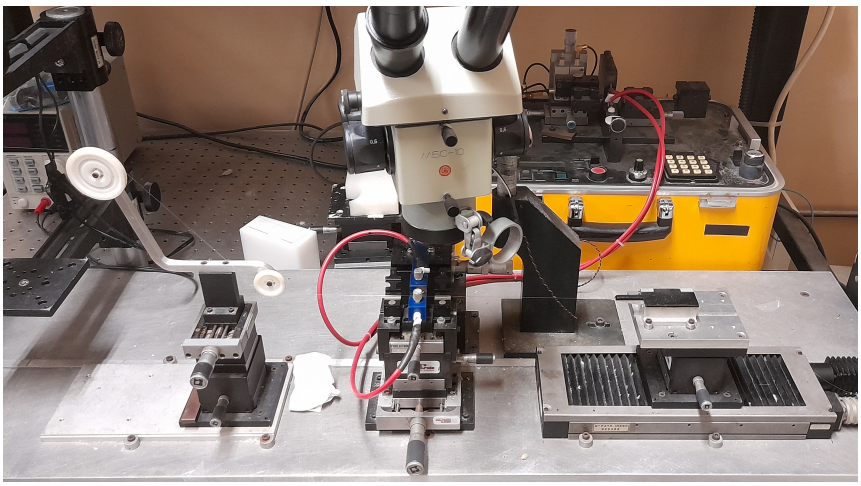

(b)

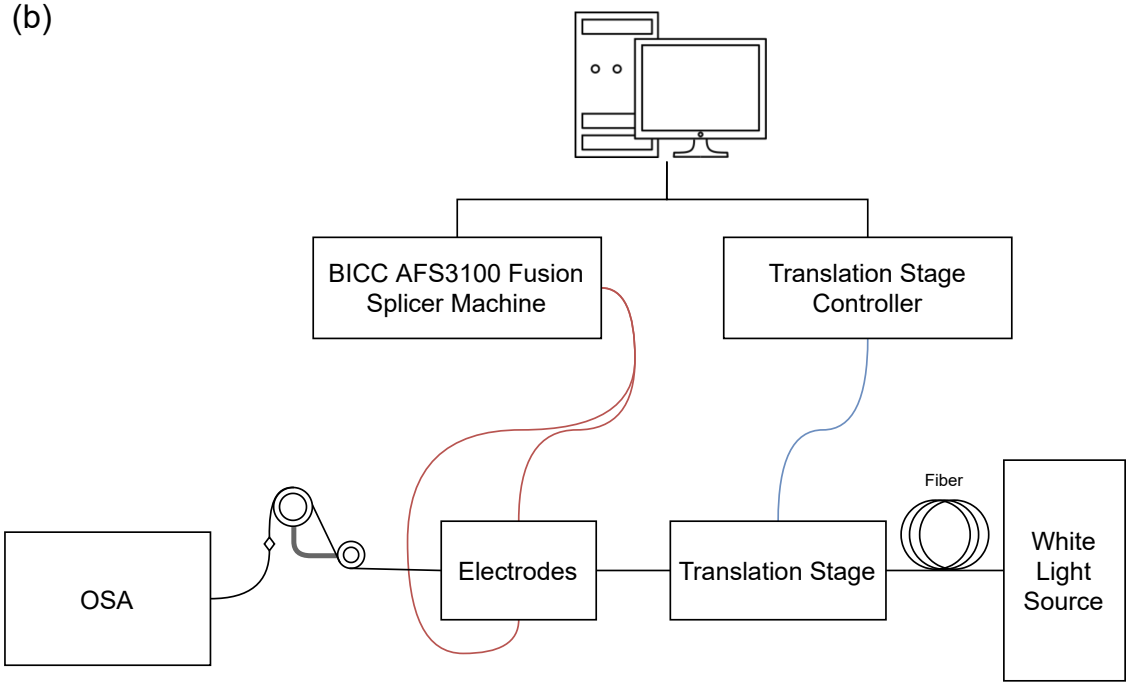

FIGURE 2.5: Fabrication setup using electric-arc where (a) shows photograph of the setup built at INESC TEC and (b) a schematic diagram of the setup.

fiber is not only low-cost, but also has a low attenuation coefficient in the infrared range, which makes it ideal for the interrogation unit to be developed.

The procedure for fabrication with this setup begins with stripping the coating of the fiber in the region where the LPFG will be created. The fiber is then placed between the electrodes which are about 1mm apart. The micrometric screws are used to align the fiber in the vertical axis with the tips of the electrodes.

As seen in the procedure described in [23], the best results are obtained with discharges between 0.2 and 0.7 seconds and currents between 8.5 and 10mA. After a discharge the fiber is displaced by the translation stage by an amount equal to the period of the grating. These steps are repeated until the desired attenuation peak is achieved. To monitor the peak during fabrication the fiber is illuminated with a white light source and the spectrum is observed with an OSA.

2.5 Modeling Long Period Gratings

The spectrum and behavior of a LPFG can be determined using the three-layer step-index fiber geometry as seen earlier in figure 2.1. To do so, both the effective refractive indices of the guided core mode and the cladding modes need to be calculated.

2.5.1 Core Mode Effective Refractive Index

To determine the guided mode's effective refractive index the fiber geometry can be assumed to consist of only the core and an infinite cladding. Because the guided mode decays exponentially outside the core any influence from the external layer can be neglected [24]. In a single mode fiber, the dispersion relation can be written as:

$$V\sqrt{1-b}\frac{J_1(V\sqrt{1-b})}{J_0(V\sqrt{1-b})} = V\sqrt{b}\frac{K_1(V\sqrt{b})}{K_0(V\sqrt{b})} \tag{2.5}$$

where J_v and K_v are the order v Bessel and modified Bessel functions, respectively. V is the V parameter of a fiber, which determines the number of modes that propagate in the fiber. It is given by:

$$V = \frac{2\pi}{\lambda}a_1 NA \tag{2.6}$$

where λ is the propagating light's wavelength, a_1 is core radius of the fiber and NA is the numerical aperture. When $V < 2.4$ the fiber has single mode behavior. When $V \gg 2.4$ the number of modes propagating is proportional to V^2.

With the V number of the fiber, it is possible to know the modes that propagate through the fiber and their propagation constants.

Tools like python's library "ofiber" [25] easily allow for the determination of the V parameter of a fiber and the normalized propagation constant (b) for the fundamental

mode as a function of the wavelength. With the normalized propagation constant, the effective refractive index of the core can be calculated with the expression:

$$n_{eff}^{co} = \sqrt{(n_{core}^2 - n_{clad}^2) * b + n_{clad}^2} \tag{2.7}$$

The propagation constant for the fundamental mode can then be obtained with equation 2.2.

2.5.2 Cladding Modes Effective Refractive Indexes

The approach to calculate the effective refractive index of the cladding modes in a three-layer fiber was described by Tsao [26] and Erdogan [7]. A similar procedure using a matrix method for a fiber with an arbitrary number of layers was described by Ivanov et al. [27] as follows.

The solutions to the electric and magnetic fields in the fiber can be written in terms of the Bessel functions as [27, 28]:

$$E^{(z)} = i\frac{u^2}{k_0\varepsilon}(AJ_v(ur) + BY_v(ur)), \tag{2.8}$$

$$H^{(z)} = -\frac{u^2}{k_0}(CJ_v(ur) + DY_v(ur)) \tag{2.9}$$

where $k_0 = \omega/c$ is the wave number, $u = \sqrt{k_0^2\varepsilon - \beta^2}$ is the transverse wavevector component and J_v and Y_v correspond to the Bessel functions.

In matrix form it can be written:

$$\begin{pmatrix} ik_0E^{(z)} \\ -k_0H^{(z)} \\ iE^{(\varphi)} \\ H^{(\varphi)} \end{pmatrix} = \begin{pmatrix} -\frac{u_i^2}{\varepsilon_i}J_v(u_ir) & -\frac{u_i^2}{\varepsilon_i}Y_v(u_ir) & 0 & 0 \\ 0 & 0 & u_i^2J_v(u_ir) & u_i^2Y_v(u_ir) \\ \frac{\sigma}{r\varepsilon_i}J_v(u_ir) & \frac{\sigma}{r\varepsilon_i}Y_v(u_ir) & -u_iJ_v'(u_ir) & -u_iY_v'(u_ir) \\ -u_iJ_v'(u_ir) & -u_iY_v'(u_ir) & \frac{\sigma}{r}J_v(u_ir) & \frac{\sigma}{r}Y_v(u_ir) \end{pmatrix} \begin{pmatrix} A_i \\ B_i \\ C_i \\ D_i \end{pmatrix} \tag{2.10}$$

where $\sigma = \beta v/k_0$ and the index i corresponds to the fiber layer being used.

The propagation constants for the various modes are the solution of the equation can be obtained by $det(N) = 0$, where N is a matrix built by elements from the various M_i matrices. A more thorough determination of this matrix can be found in [27] and appendix A.

With the effective refractive indexes of the core mode and the cladding modes the resonance condition from expression 2.4 can be visualized using a phase match graph such as the one displayed in the figure 2.6. In such a graph, an horizontal line intercepts the curves at the resonant wavelength which would generate an attenuation peak.

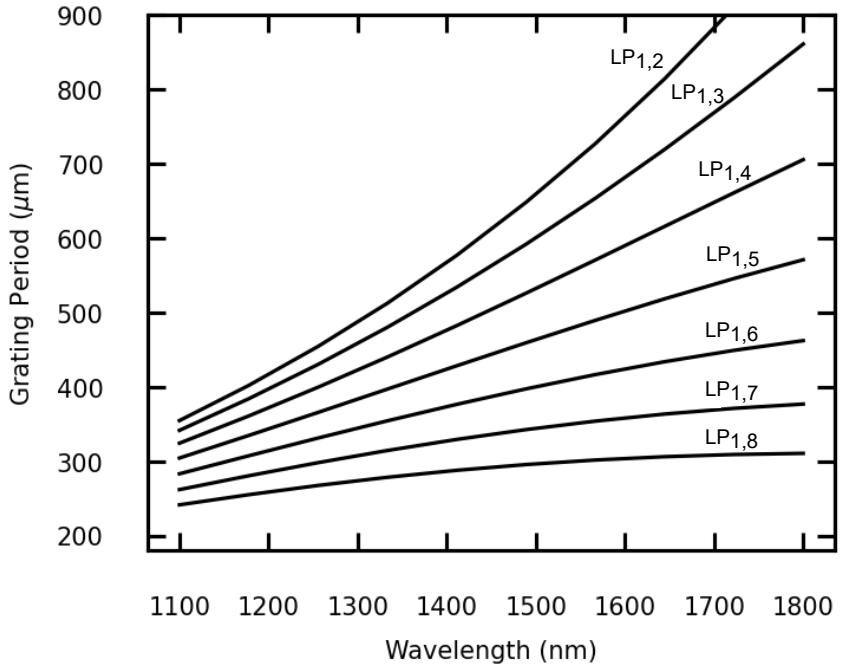

FIGURE 2.6: Phase-match condition graph determined from the effective refractive indexes of the core and seven of the cladding modes. This shows the relationship between the grating period and the attenuation peaks' wavelength.

2.5.3 Transmission Spectrum

With both the refractive indexes of the core and cladding modes, the transmission spectrum of the LPFG can be obtained with the expression [27, 28]:

$$T = 1 - \frac{\kappa^2}{\eta^2} \sin \eta L \tag{2.11}$$

where κ is the coupling coefficient of the various modes, L is the length of the LPFG and $\eta = \sqrt{\delta^2 + |\kappa|^2}$. Here δ is the mismatch parameter given by $\delta = (\beta^{co} - \beta^{cl} - 2\pi/\Lambda)/2$.

In figure 2.7 the transmission spectrum of an LPFG obtained using this method can be seen.

The same procedure can be used with different external refractive indexes. Figure 2.8 shows how the transmission peak shifts with a refractive index change ranging from

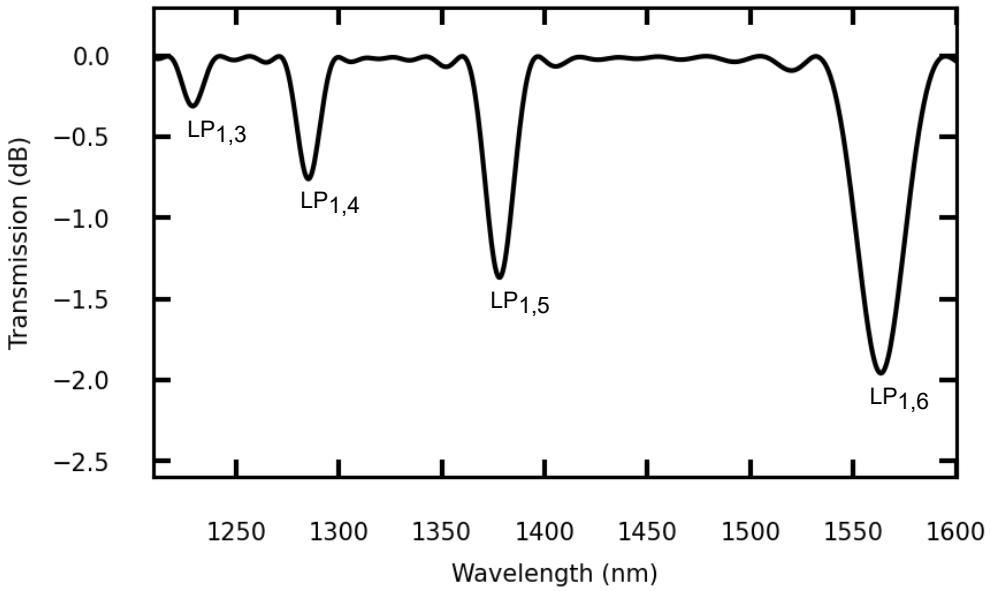

FIGURE 2.7: Transmission Spectrum of a LPFG obtained using the matrix method.

1.333 to 1.368 which correspond to the refractive index of water solutions with different concentrations of salt.

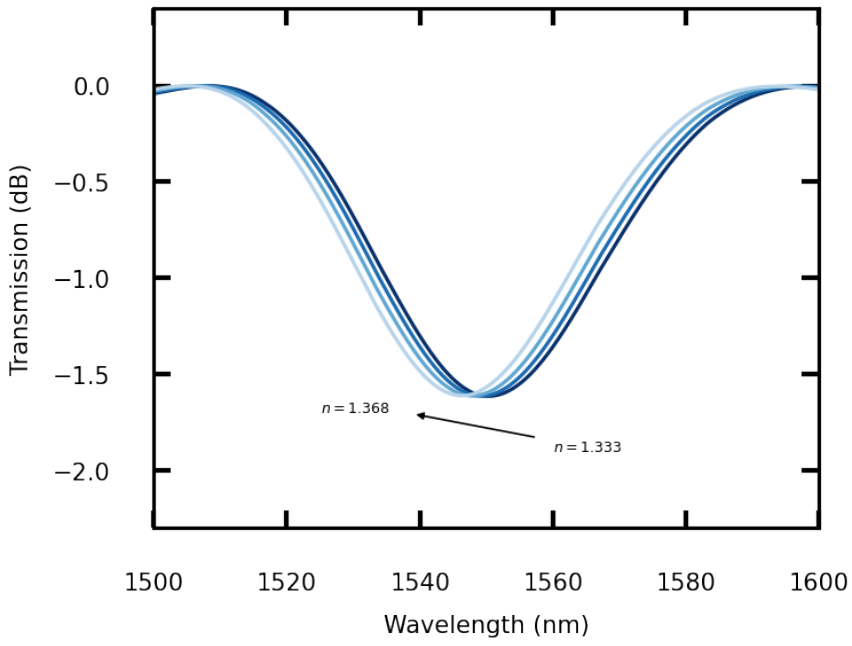

FIGURE 2.8: Effect of external refractive index changes on the LPFG spectrum as predicted by the used matrix method.

It shows a sensitivity of 114.54nm/RIU which is similar to results obtained experimentally for uncoated LPFGs in this wavelength region such as in [29].

2.6 Interrogation Methods

The most common method for the interrogation of LPFGs involves the use of an OSA which are capable of obtaining the spectrum in a large wavelength range with good resolution. For LPFGs in specific, the spectrum can be obtained by first acquiring a reference signal of the light source without the LPFG and then subtracting to the signal with the LPFG. This way, after a reference is obtained the LPFG spectrum can be monitored as desired.

The main drawbacks of using OSAs are the price of the units and how bulky and heavy they are, which make them unsuitable to any work outside of a laboratory environment[30].

Some devices are designed specifically for the interrogation of FBGs, such as commercial Braggmeters. These dedicated optical interrogators present very good resolution and are more transportable than OSAs. However, they are still costly and possess relatively low wavelength range, usually below 100nm.

One low-cost alternative, shown in [31], uses three thermally modulated fiber-coupled laser diodes that sweep around a central wavelength as a means of detecting LPFGs. The signal from the laser diodes is modulated by the LPFG and then their intensities are acquired by a photodetector. Curve fitting allows for the recovery of the full spectrum of the LPFG.

Another possible procedure can be done with two or more FBGs spectrally located at the edges of the LPFG as shown in [32]. The FBGs are kept in a controlled zone, not affected by the parameter being sensed and are modulated in wavelength by piezoelectric transducers. The signals of the FBGs are obtained by photodetectors and are visualized by an electrical spectrum analyzer.

Another option is the use of tunable Fabry-Pérot filters. In this case, the filter only allows the transmission of a narrow wavelength band, determined by the gap of the cavity. The gap of the cavity can be adjusted and thus the spectrum of the light can be obtained in a step-by-step manner by measuring the intensity of one wavelength, changing the gap length, measuring the intensity of the new wavelength and so on. These devices usually have poorer resolution but are cheaper and are commonly built in MEM devices of small proportions which make them transportable [33]. Furthermore, more than one filter with different characteristics can be used in parallel in order to reach higher wavelength ranges.

Chapter 3

Fabry-Pérot Tunable Filter

3.1 Introduction

The system developed is based on Hamamatsu's "Micro-Electro-Mechanical System Fabry-Pérot Interferometer" (MEMS-FPI) Spectrum Sensor C14272 [34] which includes a tunable Fabry-Pérot filter followed by an InGaAs photodiode and works in a spectral range of 1350nm to 1650nm. This spectral range captures a good portion of the infra-red spectrum, including the C and L bands, making this model suitable for the interrogation unit developed. This spectral range can later be expanded to 2150 nm by including additional MEMS spectrum sensors of different models such as the C13272-03 and the C14273 [35, 36].

3.2 Working Principle

The structure of the MEMS-FPI spectrum sensor is shown in figure 3.1. It is composed of a band-pass filter, a tunable filter and a photodetector. The band-pass filter rejects wavelengths outside the spectrum sensor's working range.

The tunable filter is formed by two parallel mirrors that form a Fabry Pérot cavity, as shown in figure 3.2. This cavity functions as a filter that only allows the transmission of wavelengths that satisfy the condition:

$$d = m\frac{\lambda_p}{2} \tag{3.1}$$

where d is the gap between the mirrors, m an integer and λ_p is the transmission peak wavelength.

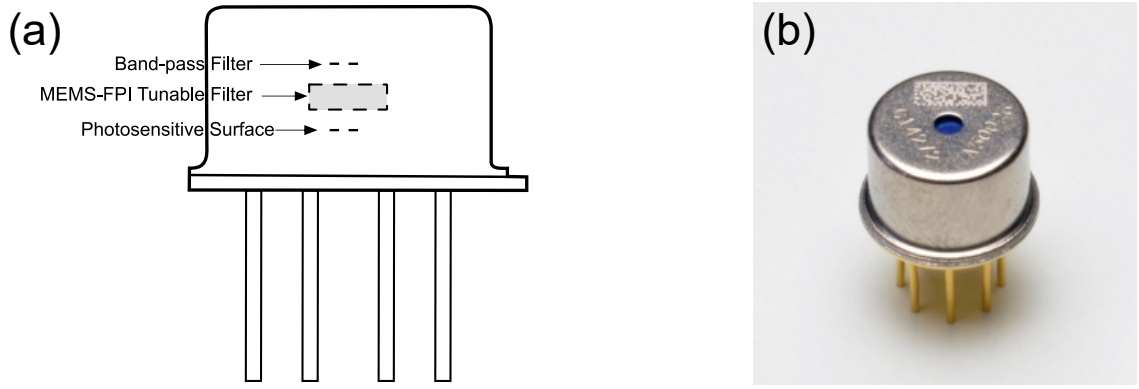

FIGURE 3.1: Structure of the MEMS-FPI spectrum sensor. On figure (a) is a diagram showing the internal structure of the device. Figure (b) shows a photograph of the MEMS-FPI spectrum sensor (adapted from the datasheet [34]).

This means that the peak of the transmission wavelength depends on the gap between the mirrors. In the MEMS-FPI this gap can be adjusted by applying a voltage between the mirrors. This voltage generates an electrostatic force that causes the upper mirror to be attracted to the lower mirror and decrease the gap. As shown in figure 3.2, a decrease in the gap causes the transmission peak to blue-shift as lower wavelengths satisfy the condition 3.1.

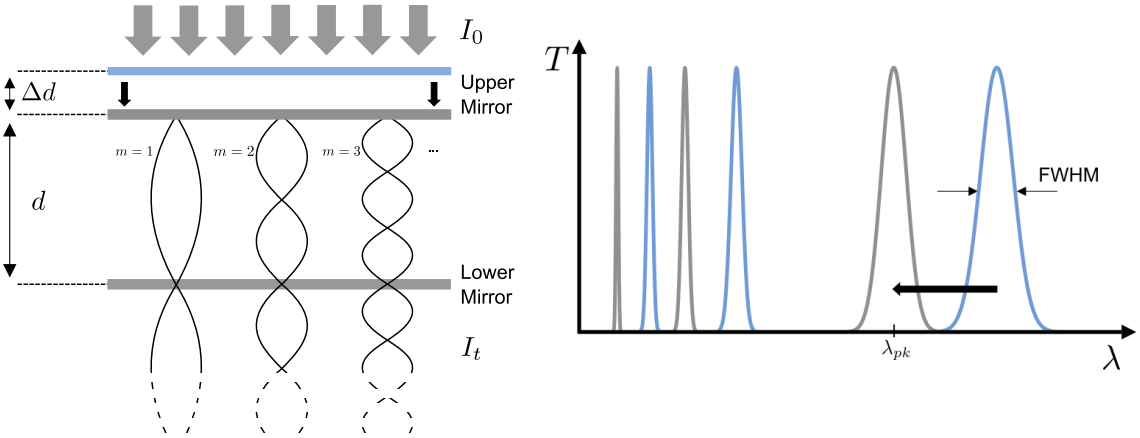

FIGURE 3.2: Working Principle of the Fabry-Pérot tunable filter. It is shown how wavelengths that resonate with the cavity are transmitted and how a change in the gap length provokes a shift of the transmission spectrum. Adapted from [33].

3.3 Filter Control Voltage

The curve that relates the peak transmission wavelength and the voltage at the filter is shown in figure 3.3. This curve is individual for each device and can be obtained using the

equations described in the datasheet and calibration constants provided with the MEMS-FPI spectrum sensor.

The MEMS-FPI spectrum sensor contains a 10K thermistor since its characteristics depend on the temperature. The calibration equations take the temperature as an input, so the peak transmission wavelength can be determined accurately.

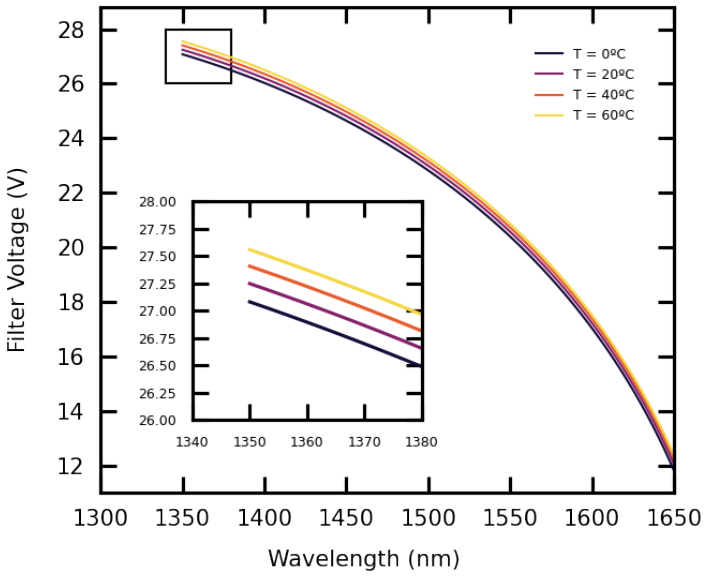

FIGURE 3.3: Relationship between peak transmission wavelength and the filter control voltage for various temperatures, as given by the individual calibration expressions for the MEMS-FPI spectrum sensor being used. The zoomed-in area shows a close up of the most temperature sensitive region.

3.4 Impulse Responses

As a response to an impulse the filter transmits a peak centered in the transmission wavelength it is set to. The spectral resolution of the MEMS spectrum sensor is considered to be the the Full Width at Half Maximum (FWHM) of the transmission peak as seen in figure 3.2. The FWHM changes with wavelength as the top mirror is slightly warped due to stress and the finesse of the cavity is lowered [37].

Using a tunable laser (Newport New Focus TLB-6700, USA) with a working range from 1520 to 1570nm several impulse responses were estimated. To obtain the curves in figure 3.4 (a) the tunable filter was fixed at a certain wavelength and the laser set at 1.0mW sweeped at a rate of 0.10 nm/s. The resulting signal was fitted to a gaussian curve to obtain the standard deviation and the FWHM shown in figure 3.4 (b).

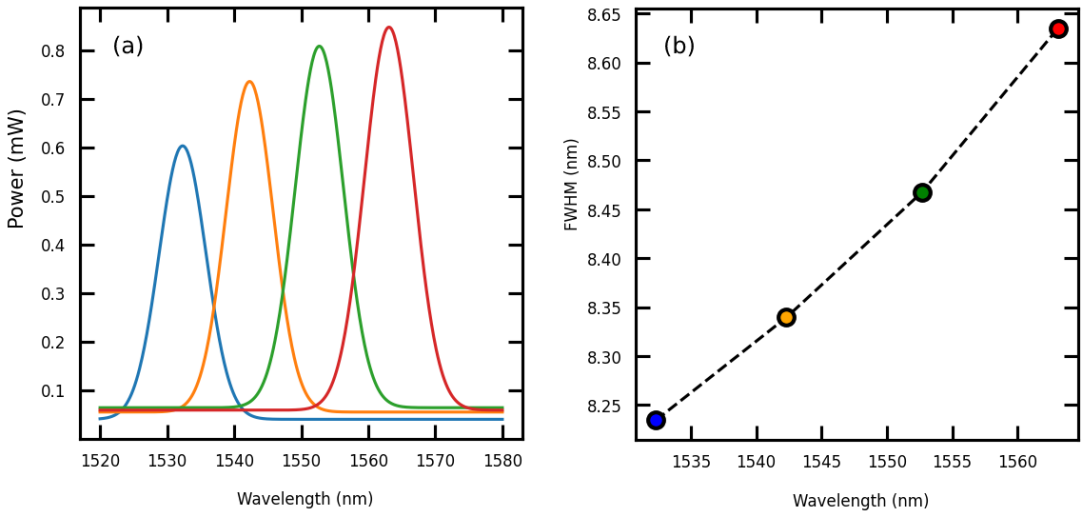

FIGURE 3.4: Impulse responses of the MEMS-FPI spectrum sensor. Graph (a) shows the curves obtained by gaussian fitting of the data acquired by sweeping the laser at various wavelengths. Graph (b) shows the FWHM of the curves.

It can be seen that, in this limited region, the transmittance of the filter increases with the wavelength which coincides with the typical responses present in the MEMS-FPI spectrum sensor's datasheet [34]. The FWHM, or the spectral resolution, also increases as expected. However, values from 8.25 to 8.65nm are seen, which are lower than the presented in the typical example of the datasheet for this region.

Any signal measured by the MEMS device's photodetector will be affected by the impulse response and suffer a convolution. Because of this, deconvolution was studied as a way to minimize the influence of the device's response function and obtain a better estimate of the real signal.

3.5 Deconvolution by Wiener Filtering

The measured signal by the photodetector is given by the convolution of the impulse response of the device and the real input signal, as seen in the expression [38]:

$$y[n] = x[n] * h[n] + \xi[n] \tag{3.2}$$

where $y[n]$ is the measured spectrum, $x[n]$ the real spectrum, $h[n]$ the instrument response function and $\xi[n]$ the noise.

In the Fourier domain, equation 3.2 can be written as:

$$Y(\omega) = X(\omega)H(\omega) + N(\omega) \tag{3.3}$$

where $Y(\omega)$, $X(\omega)$, $H(\omega)$ and $N(\omega)$ are the Fourier transforms of $y[n]$, $x[n]$, $h[n]$ and $\xi[n]$, respectively.

If $h[n]$ is known, an estimate of the input signal, $\hat{x}[n]$, can be obtained through deconvolution of $y[n]$ and $h[n]$.

In general, $H(\omega)$ tends to zero in higher frequencies. Because of this, $1/H(\omega)$ tends to infinity and the deconvolution tends to diverge.

Because of this a filter or truncation function is necessary such that the estimate of the input signal, in the Fourier domain, is given by [39]:

$$\hat{X}(\omega) = [W(\omega)/H(\omega)]Y(\omega) \tag{3.4}$$

where $W(\omega)$ is the filter.

A simple and commonly used filter is the Wiener filter, given by [38, 40]:

$$W(\omega) = \frac{H^*(\omega)}{|H(\omega)|^2 + Q^2} \tag{3.5}$$

where $H^*(\omega)$ is the conjugate of $H(\omega)$ and Q is the noise desensitizing factor. This parameter is directly related to the power spectral density of the signal and noise and is given by $1/SNR$. Because it is impractical to calculate the SNR, a commonly used estimate is given by [38]:

$$Q^2 = 10^{-2}|H(\omega)|^2_{max} \tag{3.6}$$

Errors in the estimation of the real signal will come from the fact that the impulse responses obtained, shown in figure 3.4, are also estimates and limited to that small region of the working range. Since the impulse responses change with the wavelength, signals with a wide wavelength should be deconvoluted interactively, using the various impulse responses. If the region of interest is only a small part of the spectrum, such as in the case of an LPFG attenuation peak, it can be assumed that the MEMS's response doesn't change significantly and a single central impulse response can be considered for the deconvolution.

Furthermore, because the relation between the filter control voltage and the peak transmission wavelength is not linear, as seen in section 3.3, the data acquired is not

linearly spaced. The fast fourier transform algorithm assumes evenly spaced data, and because of this an interpolation is necessary to treat the signal before deconvolution.

The experimental results of deconvolution are discussed in section 5.2.

3.6 Optimization of Light

To couple the light from the fiber to the MEMS-FPI spectrum sensor, initially, a custom 3D printed piece was designed and built to hold a FC-PC connector in place, perpendicular to the device's window. A figure showing this configuration can be seen in appendix B. However, because smf-28 fiber has a numerical aperture (NA) of 0.14 and the spectrum sensor's photosensitive area is located 3.77mm from the window, only a small portion of the transmitted light is detected due to the divergence of the beam as seen in figure 3.5 (a). To increase the amount of light that reaches the photosensitive area, which has a diameter of 0.3mm, different ways to collimate the beam at the spectrum sensor's window were studied.

3.6.1 Sphere Lens

The collimation of the beam from the fiber tip to the spectrum sensor's window was studied with the use of sphere lens (Edmund Optics, USA). A collimated beam going through a sphere lens will be focused on the lens' Back Focal Length (BFL) [41]. Similarly, a divergent beam originating from the the BFL of the sphere lens will be collimated.

The BFL of a sphere lens is given by:

$$BFL = \frac{nD}{4(n-1)} - \frac{D}{2} \tag{3.7}$$

where n is the lens' refractive index and D is its the diameter.

The software WinLens3D Basic [42] was used to simulate the setups using spheres with 2mm or 5mm diameter and made of silica glass. For a 2mm diameter lens the BFL is located at around 0.6mm, which means that with a fiber with NA = 0.14 placed at this distance the beam is collimated as seen in figure 3.5 (b). The beam diameter is only slightly larger than the spectrum sensor's photosensitive area, which means a lot less light is lost. A higher diameter lens would cause the beam diameter to be larger, so it would also increase the losses.

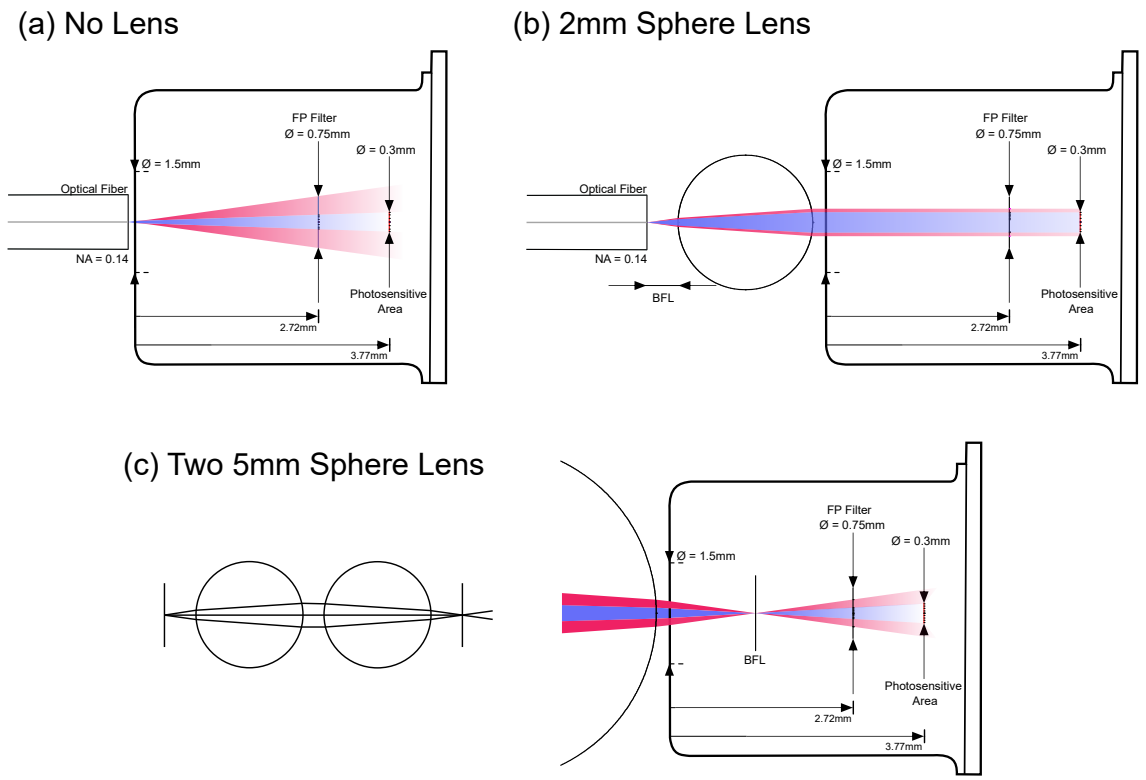

FIGURE 3.5: Simluations obtained in WinLens3D Basic for various coupling setups. Figure (a) shows the expanding beam of a fiber as it travels to the MEMS-FPI spectrum sensor's photosensitive area. Figure (b) shows the collimation of the beam by placing the fiber at the BFL of a 2mm silica sphere lens. Figure (c) shows the double sphere setup which is commonly used for fiber coupling, using 5mm silica sphere lenses.

Another common setup with sphere lens consists of two spheres in succession where the first collimates a beam originating from a light source at its BFL and the second sphere focuses the beam at its BFL [43]. With the 5mm lens the BFL is located at about 1.5mm. This setup can be seen in figure 3.5 (c). Because the MEMS's photosensitive area is further than the BFL the beam starts diverging before it reaches the photosensitive area. This setup was deemed impractical since the first setup only uses one lens and seems to have better results.

The single sphere lens still has its drawbacks. A 3D printed support was created to hold the sphere and the fiber in place at the BFL. However, high precision is needed and the resolution of the 3D printer was not enough to guarantee the alignment of the system. Experimentally an increase in the signal intensity was seen, but the control was found to be difficult.

Because it was hard to guarantee the positioning and orientation of the components of the system, more practical alternatives to the sphere lenses were studied.

3.6.2 Gradient Index Lens

A Gradient Index Lens (or GRIN Lens) is a lens with a gradual variation of the refractive index in the radial direction. These lens usually have a cylindrical shape and are commonly used in applications such as collimation, fiber coupling and beam focusing.

These lenses can be fused to a fiber to act as a collimator [44]. Experimentally with a GRIN lens (Go!Foton, USA), similar results to the single sphere lens setup were obtained. When using both the GRIN lens and the sphere lens a radial asymmetry in the power read was noticed. It was hypothesized that the photosensitive area is not precisely centered, since the MEMS's datasheet indicates that its position has a $250\mu m$ error in relation to the center.

To study the profile of the intensity read by the MEMS as a function of the horizontal position in front of the MEMS's window, a translation carriage with micrometric screws was used to sweep horizontally both the bare fiber and the fiber with the GRIN lens. The fiber was illuminated using a C+L bands light source and the MEMS was fixed reading the intensity at 1550nm. The results can be seen in figure 3.6.

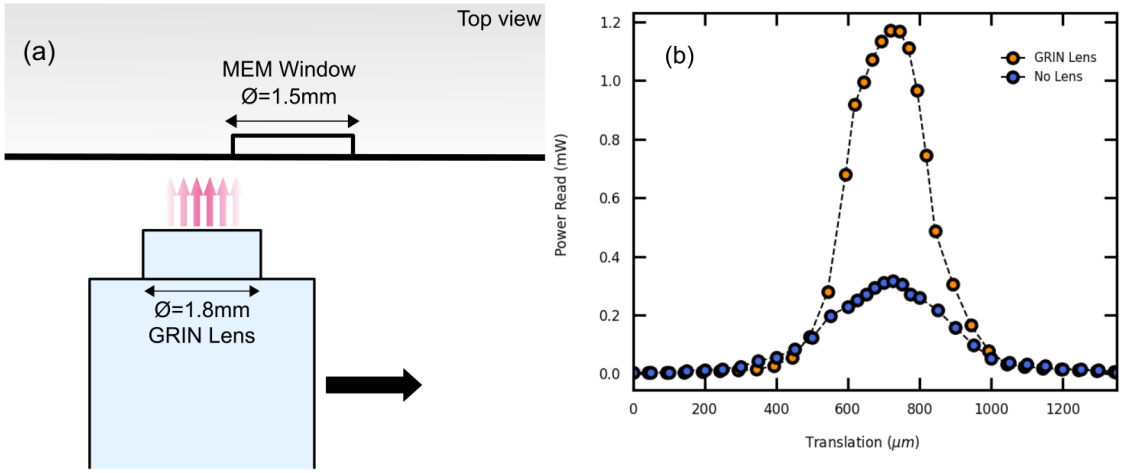

FIGURE 3.6: Sweep of the window of the MEMS-FPI spectrum sensor with and without a GRIN Lens. Figure (a) shows a diagram of the setup as the the GRIN lens is translated across the MEMS's window. The graph shown in (b) shows the results obtained, where the y-axis shows the power read by the MEMS-FPI spectrum sensor and the x-axis shows the position of the fiber and GRIN lens in the horizontal axis of the window.

The increase in the intensity of the signal read can be clearly seen, however no quantitative conclusion can be made since the y-axis represents the power read by the photodetector, which depends on it's calibration. By fitting the results to gaussian curves it can be seen that the GRIN lens curve has FWHM of $251.6 \pm 0.1\mu m$ and the bare fiber shows $371.5 \pm 0.1\mu m$. The shorter FWHM of the GRIN lens curve might indicate a smaller beam

diameter as we would expect from the collimated beam, because it is expected the curves are the result of the convolution of the beam with the photosensitive area.

This setup is more practical than the single sphere lens setup since it isn't dependent on the distance of the fiber to the BFL of the lens, which is hard to control. Furthermore, the increase in the signal intensity means that the power range the device can read is increased, which is specially relevant for measurements with low optical power to increase the signal-to-noise ratio.

Chapter 4

Interrogation System Development

4.1 Introduction

The interrogation unit developed uses the MEMS-FPI spectrum sensor described in chapter 3. The unit was designed to be portable, compact, and low-cost. It allows for the interrogation of optical fiber sensors in the working range of the MEMS-FPI, from 1350 to 1650nm. The interrogation unit is shown in figure 4.1.

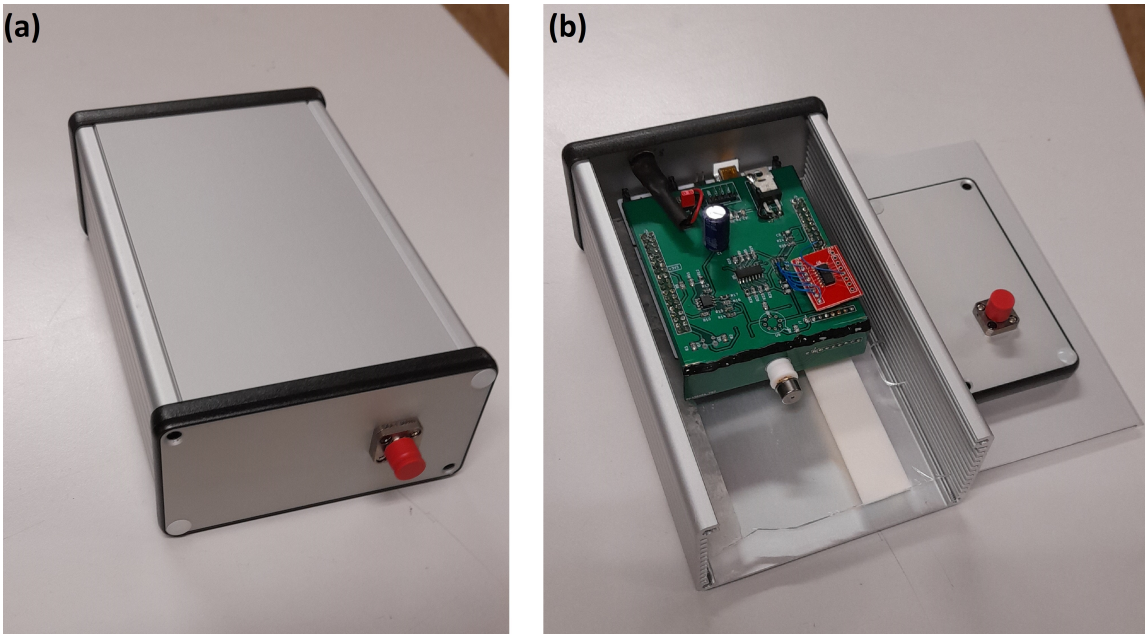

FIGURE 4.1: Image of the developed interrogation unit: (a) shows the external design and (b) shows the interior.

The unit consists of a STM32 development board Nucleo microcontroller [45] with a dedicated Printed Circuit Board (PCB) acting as a shield.

The PCB shield was designed to include a power supply circuit which is powered by a 30V DC transformer, thermistor voltage dividers, a voltage amplifier circuit and a current amplifier circuit with eight preset gain values. The voltage amplifier circuit amplifies the voltage from the microcontroller's DAC to the desired filter control voltage. The current amplifier circuit amplifies the signal from the MEMS's photodetector to be read by the microcontroller's ADC.

The microcontroller board is linked directly to a computer or Raspberry Pi through a USB connection. A diagram of the layout can be seen in figure 4.2.

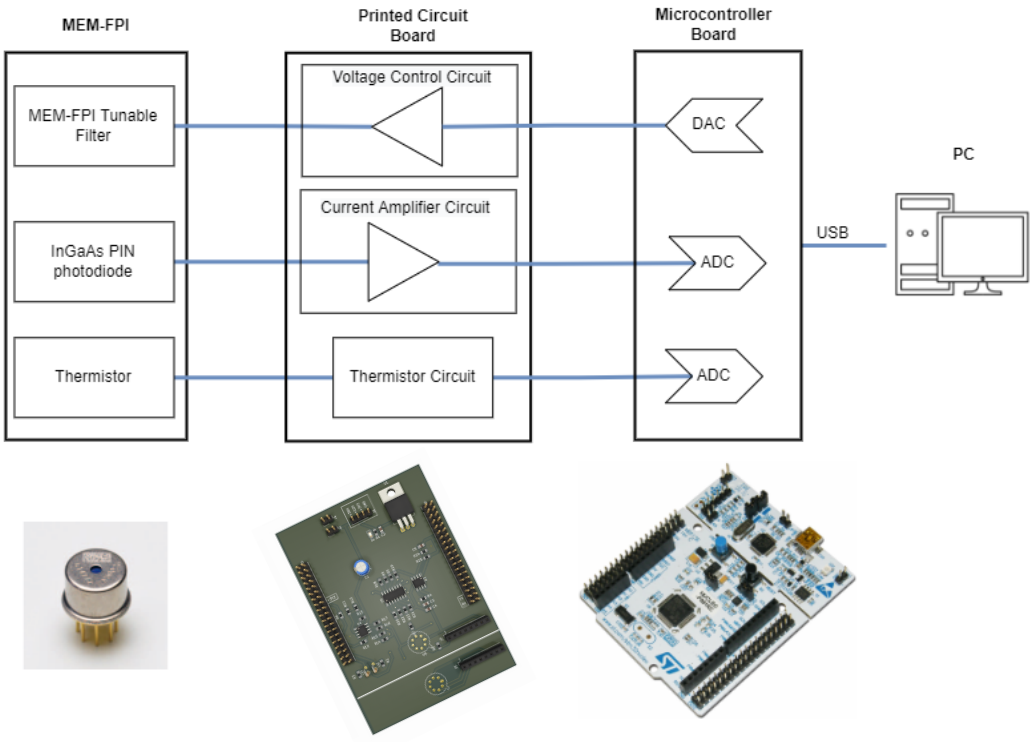

FIGURE 4.2: Diagram layout of the developed interrogation unit showing the connections between the various components of the system.

The MEMS is connected by a socket to the PCB. The optical connection is made by a 3D printed piece that allows the GRIN lens to be placed in parallel to the MEMS's window. The fiber fused to the GRIN lens has an FC- APC connector which is connected to the internal side of the fiber panel adapter in the case which can be seen in figure 4.1.

The data acquisition is made through the USB connection. A developed user interface allows for the control of measuring settings and the visualization of the acquired data in the computer.

4.2 Microcontroller Board

The main characteristics considered when choosing the microcontroller board were the cost, portability, power consumption and ADC/DAC resolution. In the DAC, at least a 12bit resolution was desired since that would allow for steps of 0.8mV in the 0 to 3.3V range. After the amplifier circuit this allows steps of around 3.7mV in the range of the filter control voltage. In the FPI tunable filter, a change of 3.7mV in the control voltage is the equivalent of a change in peak transmission wavelength from 0.03 to 0.2nm depending on the region of the spectrum. The step in wavelength is not constant in wavelength for the same voltage step because the relation between the filter voltage and the peak transmission wavelength is not linear as was shown in section 3.3.

The microcontroller chosen for the interrogation unit is the STM32F091RC Nucleo development board [45]. This board contains 16 ADC channels with 12bit resolution, enabling the acquisition of several points at each step and averaging, all while keeping the measuring time low. It also possesses 2 12bit DAC channels. This board can be programmed using C language and has built-in communication functions which allow for easy use of communication interfaces such as, for example, the UART, SPI and I2C protocols. Due to these characteristics and it being relatively cheap and compact, this board is an ideal option for the developed system.

4.3 Printed Circuit Board

This PCB was designed using the open-source software, KiCad [46]. It is powered by a 30V DC transformer and it is connected as a shield to the STM32 microcontroller board. The MEMS-FPI spectrum sensor is connected to a socket in the PCB, which allows it to be easily replaced. The PCB can be seen in figure 4.3. A full schematic of the PCB can be seen in appendix B.

4.3.1 Voltage Amplifier Circuit

This circuit is responsible for regulating the filter control voltage. It is shown in figure 4.4 and it consists of two amplifier setups in series.

The amplifiers in this case are powered by the 30V line of the circuit. The signal generated by the microcontroller's DAC originates a voltage between 0V and 3.3V which is amplified by a gain given by $1 + (R_{12}/R_{11})$ which equals 5.2.

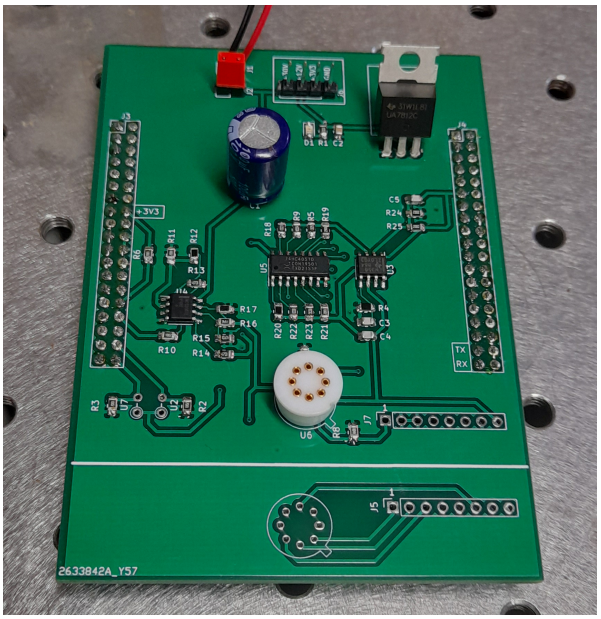

FIGURE 4.3: Photograph of the Printed Circuit Board developed.

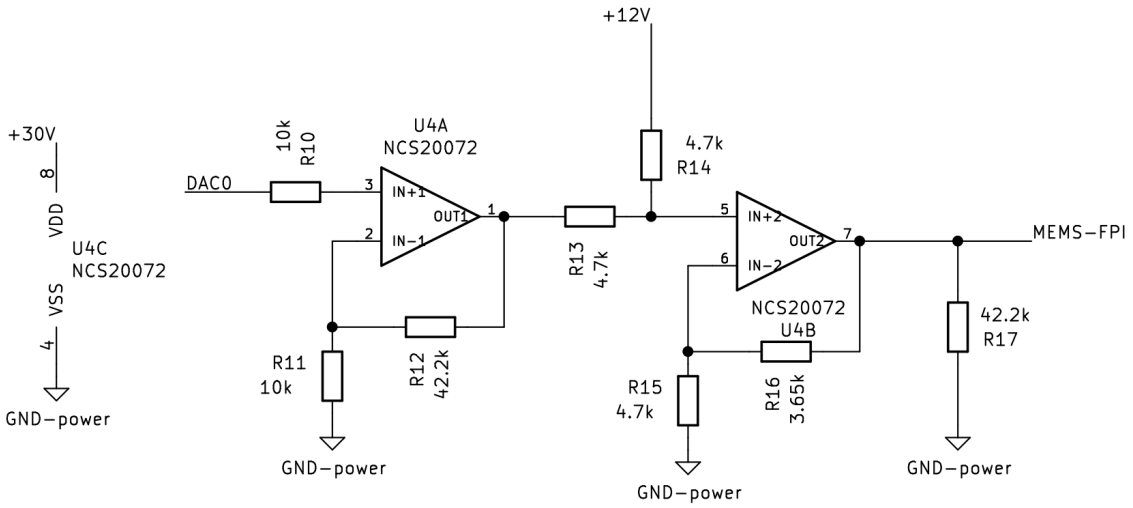

FIGURE 4.4: Voltage Amplifier Circuit schematic.

The second amplifier provides a gain given by $1 + R_{16}/R_{15}$ which equals 1.78.

Between the amplifiers there is a voltage divider with a 12V reference voltage. The resulting voltage offsets the output signal so that when the DAC is at 0V the input at the second amplifier is at 6V. The resulting output is 10.72V when the DAC is at 0V and 25.96V when the DAC is at 3.3V.

If the filter is subjected to voltages higher than its absolute maximum, a phenomenon known as "pull-in" happens where, due to the electrostatic force, the mirrors are pulled together and springs on the upper mirror are irreversibly damaged. The voltage of this

circuit was capped at 25.96V to increase the safety margin, however this limitation reduces the spectral range of the system. In the individual MEMS-FPI spectrum sensor used, the range is limited from around 1380 to 1650nm.

Experimentally, the relation between the DAC value and the voltage at the output of the circuit was obtained by varying the DAC value and measuring the output with a multimeter. The result can be seen in figure 4.5.

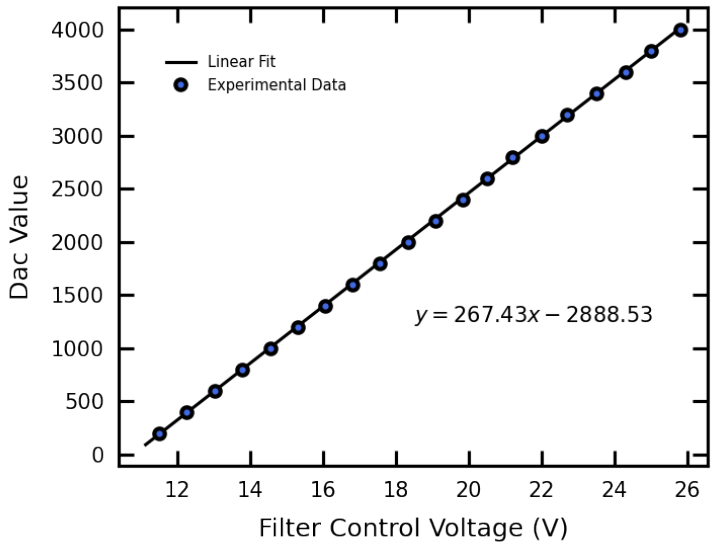

FIGURE 4.5: DAC to Filter Control Voltage Calibration.

The obtained relation is used by the microcontroller to set the filter control voltage as desired during data acquisition.

4.3.2 Current Amplifier Circuit

The current signal from the spectrum sensor's photodetector is acquired using the circuit shown in figure 4.6. The signal is amplified by a gain which is determined by a 1:8 multiplexer.

At each of the multiplexer's outputs there is a different resistor that determines the gain applied to the circuit due to the first amplifier. This gain is chosen by the microcontroller. If the signal at the microcontroller's ADC is too low, it switches the multiplexer to a higher resistor output which increases the gain. If the ADC is close to saturation, a lower value resistor is chosen, decreasing the gain.

Precision amplifiers, model AD8552, were chosen for their low off-set voltage ($1\mu V$) and low input bias current ($20pA$). These characteristics are important because the off-set

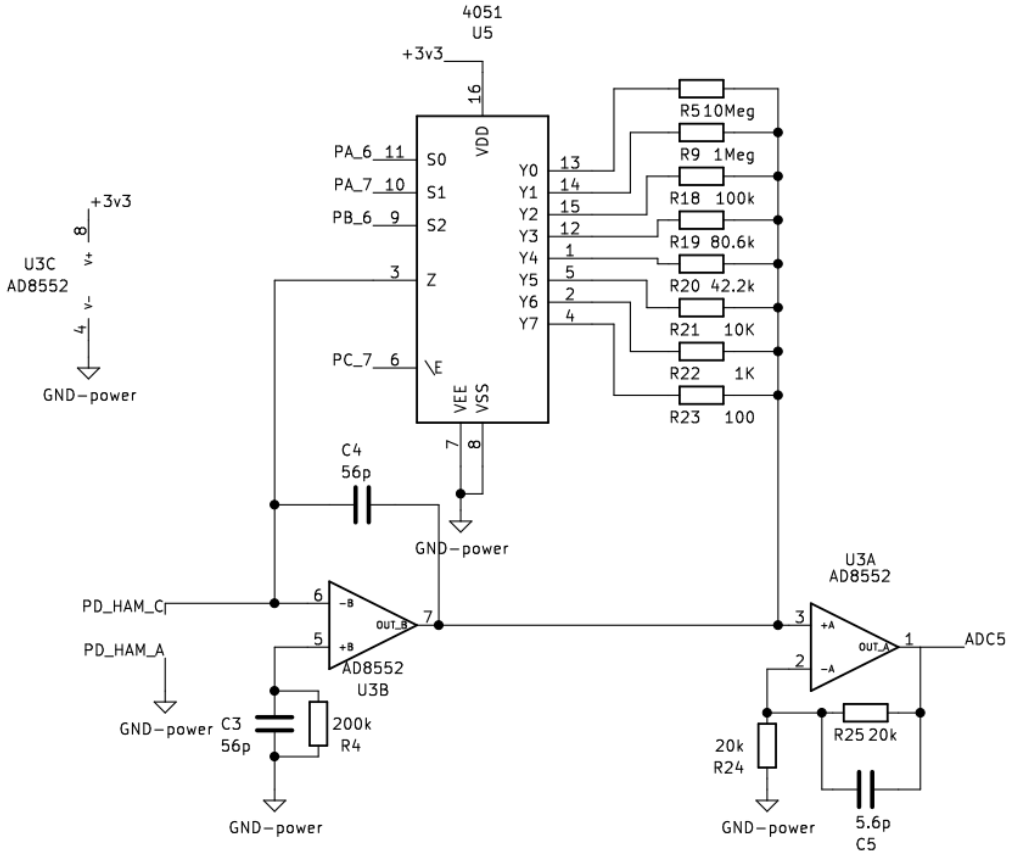

FIGURE 4.6: Current Amplifier Circuit with Eight Gains.

voltage error increases with the gain and the largest gain in the circuit is given by the $10M\Omega$ resistor. It also has a high Common Mode Rejection Ratio ($130dB$) which helps to reduce the noise, specially in low power measurements where the signal-to-noise ratio is lower. The gains of the circuit were calibrated to convert the current signal from the photodetector to the optical power reaching the spectrum sensor's photosensitive area. The results are shown in figure 4.7.

The calibration was done using a tunable laser with adjustable output power (New Focus TLB-6700). The MEMS-FPI device was fixed at the laser's central wavelength, set to 1550nm. At each gain the power was changed and the value read by the ADC was compared to the reading of an optical power meter (TriBrer AOP100C, China). Only six of the preset gain values were calibrated since, at lower gains, the laser's maximum output was reached, and it is important to keep the conditions of the calibration constant to make sure there are no discontinuities between gains during measurements. At higher gains, with low output power, the laser isn't stable enough to allow for good readings. The highest gain, given by the $10M\Omega$ resistor, was calibrated separately and designed specifically for

low optical power measurements such as reading with single mode fiber and broadband white light sources.

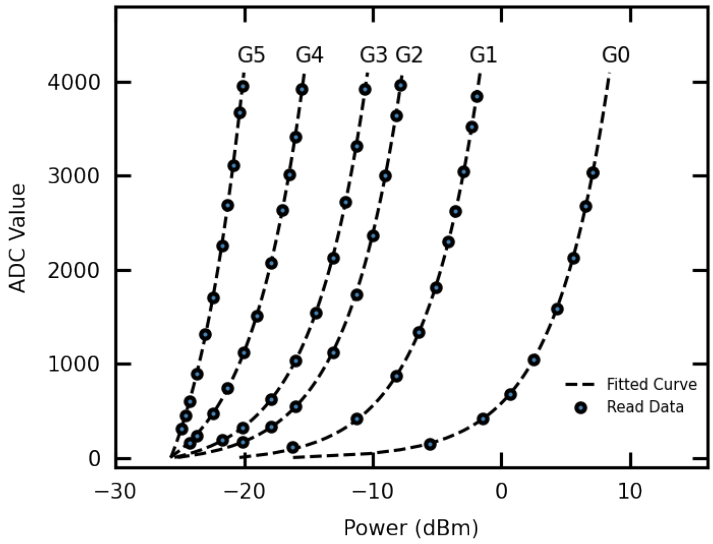

FIGURE 4.7: Optical power calibration for the different gains. Each curve shows the relation between the value read by the ADC and the corresponding optical power.

4.3.3 Thermistor Circuit

The thermistor present in the MEMS-FPI spectrum sensor is read using a simple 3.3V voltage divider circuit with a $10K\Omega$ resistor. Because the thermistor, ideally, is $10k\Omega$ at 25ºC, the ADC should read 1.65V has the 3.3V are split between the two resistors.

The MEMS-FPI spectrum sensor datasheet recommends a calibration with the Steinhart-Hart equation, given by:

$$\frac{1}{T} = A + B[ln(R_{th})] + C[ln(R_{th})]^3 + 273.15 \tag{4.1}$$

where R_{th} is the thermistor resistance and A,B and C are the calibration constants obtained experimentally.

With the ADC the thermistor resistor can be determined with the expression:

$$R_{th} = R_0 \frac{ADC}{4095 - ADC} \tag{4.2}$$

where ADC is the value read by the ADC and R_0 is the voltage divider resistor.

The calibration constants were obtained by measuring the thermistor resistance at several temperatures from 15 to 40ºC and fitting the result to the Steinhart-Hart equation. The final curve is shown in figure 4.8.

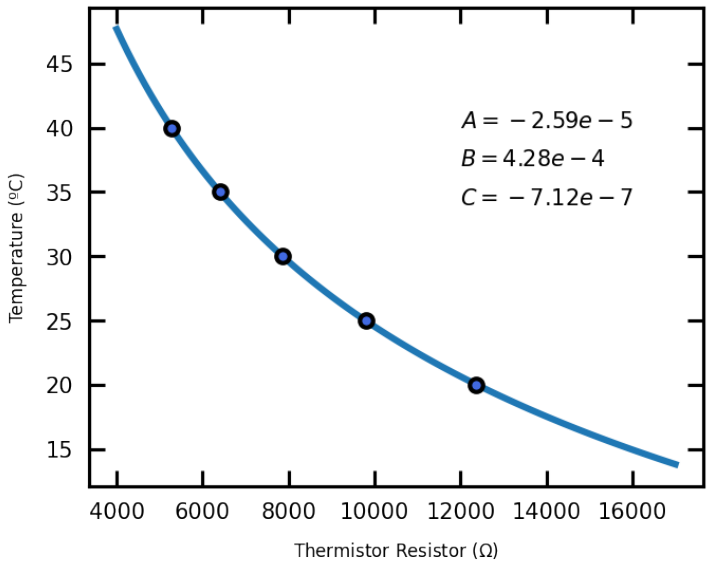

FIGURE 4.8: Thermistor calibration curve obtained by fitting the Steinhart-Hart equation.

4.4 Graphical User Interface

A graphical user interface was developed using Python's library PyQt5 [47]. An image showing the design of the interface can be seen in figure 4.9. In the interface the measurement settings can be set, such as the spectral range of the measurement, the time step between points and the DAC step. These values are communicated to the microcontroller using a simple protocol developed in the serial UART interface.

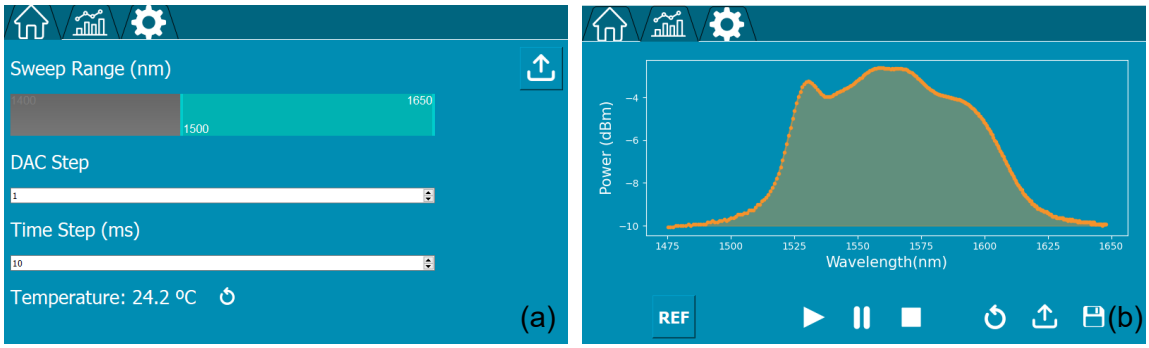

FIGURE 4.9: Graphical user interface designed with PyQt5, where (a) shows the home window where the measurement settings can be set and (b) shows the measurement window where the data can be visualized.

The interface also allows for the visualization of data acquired. Because the MEMS-FPI filter only takes up to $1ms$ to stabilize in the right transmission wavelength, the limiting time factor during acquisition is the time the interface takes to process and store the data transmitted. The data isn't plotted in real time because it would slow the measurement considerably.Instead, data is saved in a buffer and displayed all at once when the sweep is finished. Best results are obtained when at least $10ms$ time steps are allowed between points. A full spectral range sweep at the lowest DAC step takes at this rate takes about 36 seconds to acquire. In most applications the whole range is not necessary. In short ranges the spectrum can be obtained in just a few seconds.

The interface also allows for the storage of information such as default settings for all these parameters, calibration constants for the MEMS-FPI spectrum sensor in use and calibration constants for the DAC/filter control voltage curves. These settings are saved in a configuration file so that they are kept between restarts of the application. The configuration window of the interface can be seen in appendix B.

Chapter 5

Experimental Results and Discussion

5.1 Introduction

The developed interrogation unit, described in chapter 4, was designed for the interrogation of optical fiber sensors in the infra-red range, from 1350 to 1650nm. To test and validate the unit, several measurements in different conditions were performed, most comparing the results with those obtained with a commercial OSA (Yokogawa AQ6370D, Japan) working at a resolution of 2nm.

A deconvolution method was tested to minimize the effect of the impulse response of the MEMS-FPI sensor, obtaining better estimates of the input signals. The possibility of low-power applications, such as with white-light sources, was studied. Furthermore, LPFGs were used for validation and were interrogated as temperature, RI and humidity sensors.

5.2 Deconvolution

The deconvolution method described in section 3.5 was used to get an estimate of the spectrum of a light source in the C and L bands of the infra-red. The signal was acquired with the MEMS-FPI spectrum sensor and with an OSA for comparison and it can be seen in figure 5.1.

After deconvolution the signal loses optical power, as would be expected since the integration effect of the impulse response is minimized. At the edges of the deconvoluted spectrum small ringing effects can be seen, which arise due to the Gibbs Phenomenon.

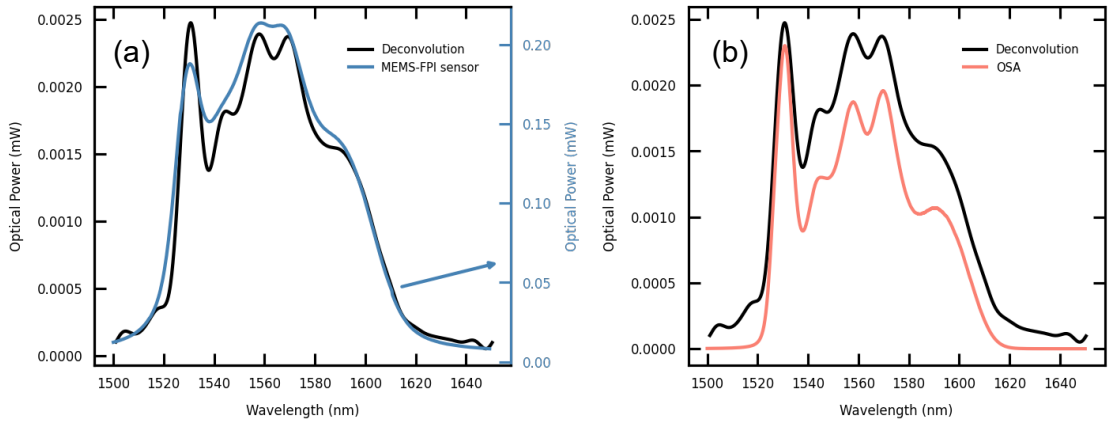

FIGURE 5.1: Deconvolution of spectra of a C and L Bands Light Source: (a) shows the comparison between the acquired spectra before and after deconvolution and (b) shows the same spectra compared to the one acquired by an OSA. Because of the large difference in scale, graph (a) presents two different scales.

The last point of the curve is not differentiable and the Fourier Transform causes some oscillatory behavior near these regions.

Visually it is possible to see an improvement in the shape of the curve when compared to the one obtained with the OSA, however a quantitative figure of merit was desired. For this, a method based on the Sum of Squares Due to Error (SSE) was designed.

First, the signals were all normalized to their respective maximums since they have very different scales. Then, the squared residuals, obtained by $R_i = (y_i - y_{OSA,i})^2$ were calculated and can be seen in figure 5.2.

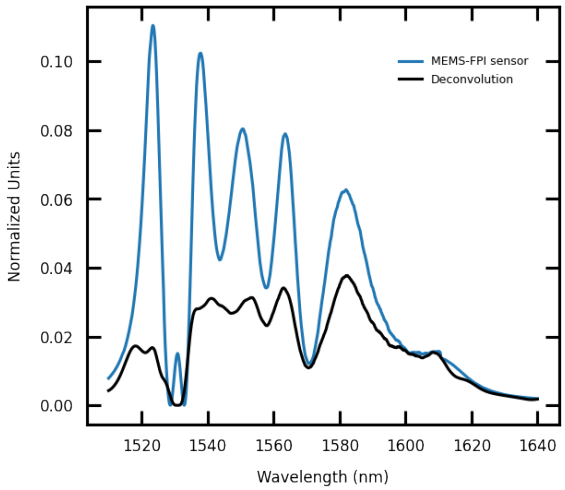

FIGURE 5.2: Squared residuals obtained from the normalized curves in relation to the OSA spectrum.

The SSE is then given by the sum of the squared residuals. SSE is closer to zero when the signal is a good approximation of the curve acquired by the OSA. For the measured signal the obtained SSE was equal to 33.67 and for the deconvoluted signal it was equal to 17.19.

With this we can quantitatively conclude that the deconvoluted signal is a closer approximation of the OSA acquired signal, however this method can be improved since the normalization of the curves to their maximum is not an ideal procedure and affects the results obtained.

A deconvoluted LPFG spectrum was also obtained in a similar fashion. In figure 5.3 a comparison between the measured signals and the deconvolution can be seen.

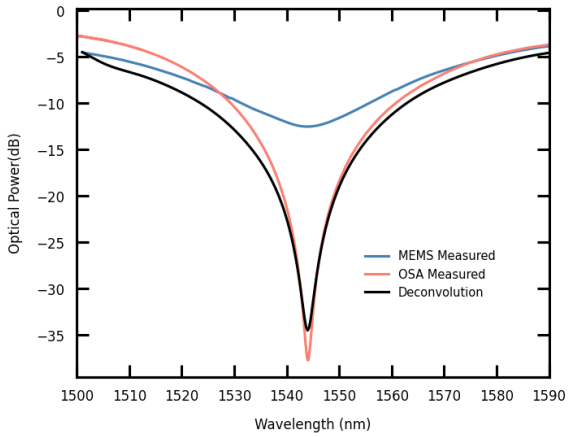

FIGURE 5.3: Deconvolution of the spectrum of an LPFG and comparison with the one acquired by an OSA.

Since one of the advantages of the developed system is the relatively large working spectral range, a similar procedure was followed using a Halogen-Tungsten white light source. The amount of light coupled into the fiber is very low, however the spectrum of an LPFG at around 1460nm was still seen in figure 5.4 (a).

There was no impulse response acquired experimentally in this region of the spectrum. For the deconvolution an estimation of the impulse response based on the typical example shown in the datasheet [34] was used. The deconvolution, shown in figure 5.4 (b), was still able to estimate the LPFG spectrum. However, in this case, the resulting signal was specially dependent on the values chosen for the noise desensitizing factor (Q). This dependence probably comes from a combination of the fact that the impulse response was not estimated experimentally and from the low optical power nature of the original signal.

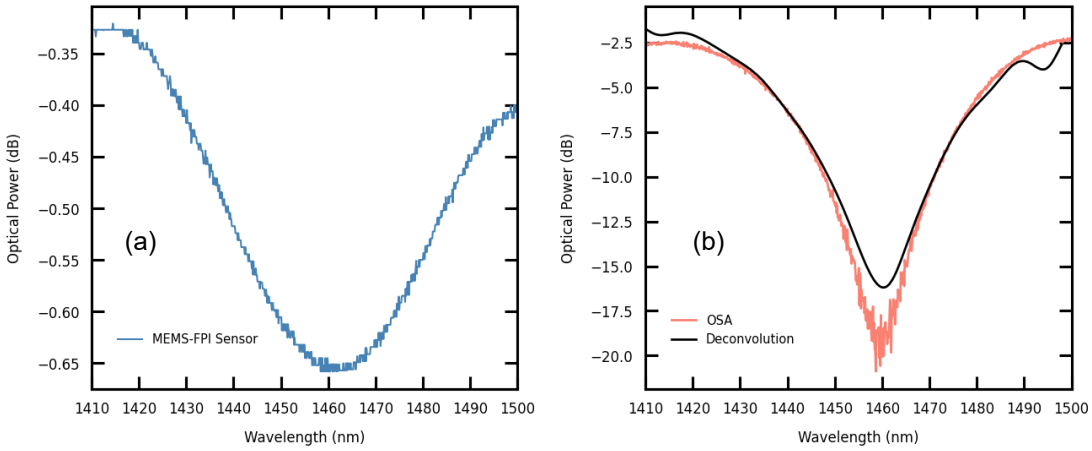

FIGURE 5.4: Spectra obtained using a Halogen-Tungsten white light source. Figure (a) shows the spectrum of the LPFG measured by the MEMS-FPI sensor. Figure (b) shows the spectrum after deconvolution, compared to the measurement made by an OSA.

5.3 Interrogation of an LPFG as a Temperature Sensor

The developed system was used to interrogate an LPFG acting as a temperature sensor. The LPFG was fabricated using the electric arc setup described in section 2.4. At ambient temperature it shows an attenuation peak at around 1545nm. It was submitted to temperatures ranging from 150 to 400°C which causes a red-shift in its spectrum as the temperature increases. The spectra were acquired both by the interrogation unit developed and an OSA. A diagram showing the setup for this measurement can be seen in figure 5.5.

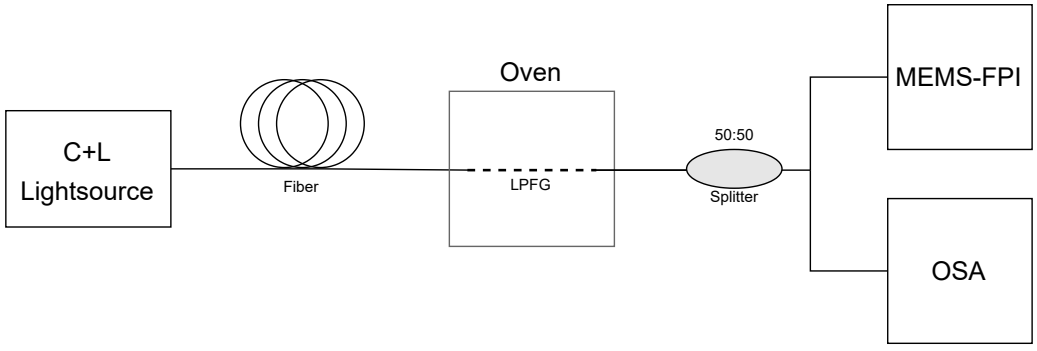

FIGURE 5.5: Setup Diagram for Temperature Measurement.

At first, a reference spectrum of the light source without the LPFG was taken. The oven (Thermolab, Portugal) is PID controlled and during the procedure all the spectra were taken after the oven fully stabilized at the set temperature. Furthermore, at each

temperature several spectra were acquired reduce the uncertainty in the peak's minimum position.

In the case of the MEMS-FPI spectrum sensor, the measured spectra were deconvoluted using the method described in previous chapters. The comparison of the results obtained by the MEMS-FPI and the OSA can be seen in figure 5.6.

The wavelength shift of the peak can be represented as a function of the temperature to obtain the sensitivity of the LPFG, given by the slope of the curve. For the MEMS-FPI sensor a sensitivity of $0.142 \pm 0.007 nm/°C$ was obtained. For the OSA the sensitivity calculated was $0.135 \pm 0.004 nm/°C$. Relative to the OSA the MEMS-FPI system shows a 4.9% error.

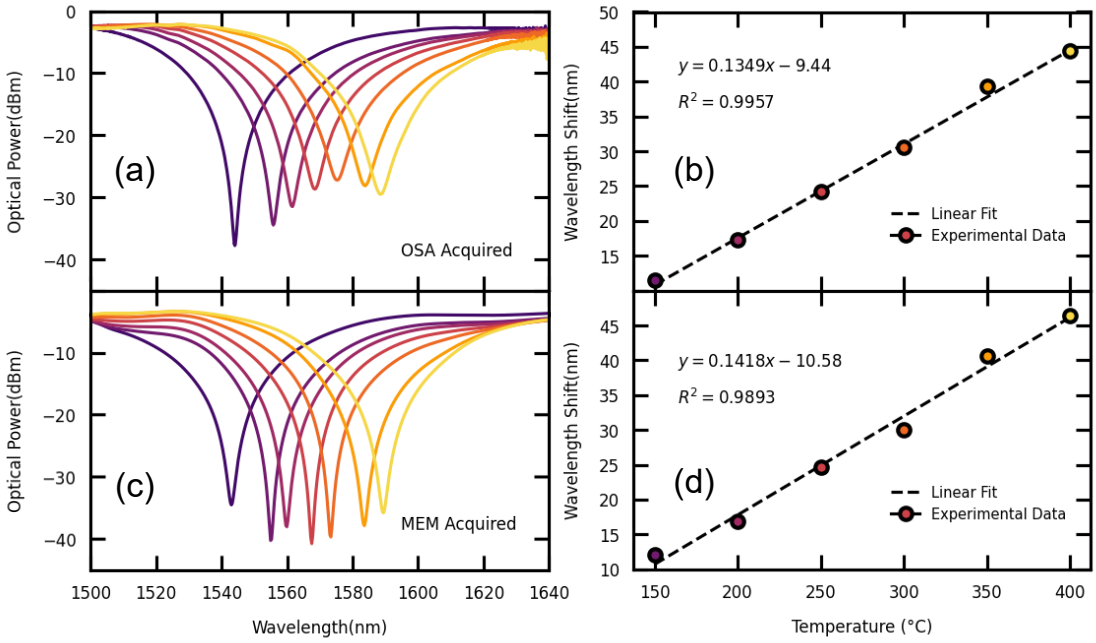

FIGURE 5.6: Spectra of an LPFG subjected to different temperatures. Figures (a) and (c) show the spectra acquired by the OSA and the MEMS-FPI system, respectively. Figures (b) and (d) show the sensitivity calculated with data from the OSA and MEMS-FPI, respectively.

5.4 Interrogation of an LPFG as a Refractive Index Sensor

The developed system was used to interrogate an LPFG as a RI sensor. An LPFG with an attenuation peak at 1600nm in air was submitted to solutions of varying RI, ranging from 1.333 to 1.366. The increase in the external RI changes the effective refractive index of the LPFG causing a blue-shift in the attenuation band.

A similar procedure to the one used for the temperature measurement was used, except instead of an oven the LPFG was submerged in solutions of different RI. The RI of the solutions was measured using a Abbe refractometer (Atago DR-A1, USA) The comparison between the results with the developed interrogation unit and an OSA can be seen in figure 5.7. Furthermore, spectra simulated using the matrix method described in section 2.5 are also shown.

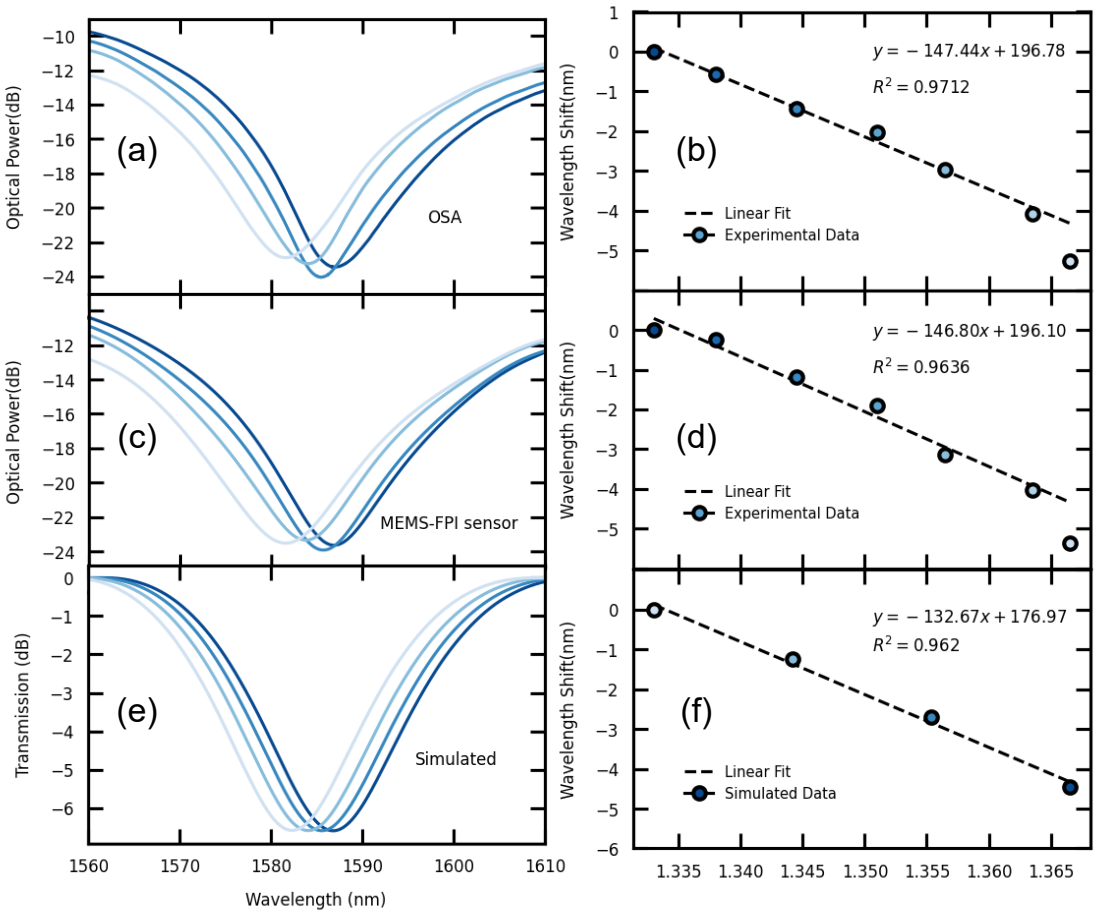

FIGURE 5.7: Spectra of an LPFG subjected to different RI. Figures (a) and (c) show the spectra acquired by the OSA and the MEMS-FPI system, respectively. Figures (b) and (d) show the sensitivity calculated with data from the OSA and MEMS-FPI, respectively. Figures (e) and (f) show results simulated in this region using the matrix method.

The sensitivity to external RI variations is presented as an approximation since the wavelength shift as function of the RI is not linear. The MEMS-FPI sprectrum sensor shows a sensitivity of 146 ± 13 nm/RIU and the OSA 147 ± 11 nm/RIU. Relative to the OSA the MEMS-FPI spectrum sensor results show an error lower than 1%. The simulation spectra give a sensitivity of 137 ± 7nm/RIU which is a good result considering the method used to obtain the spectra doesn't take into account factors such the fabrication

method.The induced electric-arc fabrication technique doesn't only affect the LPFG in the core, it also causes changes to the cladding by introducing physical deformations which influence the sensitivity and are difficult to implement in the simulations.

5.5 Interrogation of an LPFG as a Humidity Sensor

Besides the characterization of the system with an LPFG exposed to temperature and external refractive index variations the entire setup was validated to interrogate a sensor for humidity monitoring using an LPFG.

Certain polymers have RI that decreases with humidity as water molecules are absorbed. An LPFG can be coated with such a polymer to be used as a humidity sensor, since the external refractive index will affect the attenuation band of the spectrum.

The developed interrogation system was used to interrogate an LPFG coated with a water soluble polymer, Polyvinyl Alcohol (PVA). The PVA solution used consisted of water with a concentration of 10% wt/wt of PVA. The setup used for the measurement has been shown in [48]. It consists of a chamber with two valves that allow for control of the humidity inside. A DHT22 humidity and temperature sensor connected to an arduino was used to measure the relative humidity (%RH).

The results of the measurement can be seen in figure 5.8.

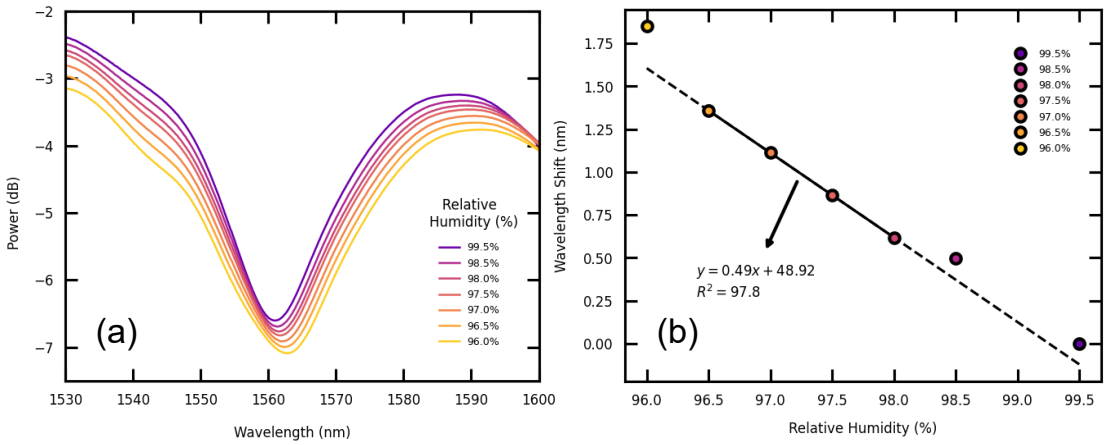

FIGURE 5.8: Spectra and sensitivity of an LPFG coated with PVA: (a) show the spectra obtained by the MEMS-FPI spectrum sensor as the relative humidity decreases and (b) shows the wavelength shift as a function of the relative humidity.

The wavelength shift is not perfectly linear with the RH, however a linear regression still allows for an estimation of the sensitivity. Four points were chosen, as seen in figure 5.8 (b), to estimate a sensitivity of 0.49 ± 0.05 nm/%RH.

This study should be repeated with a wider RH range so the behavior and phenomena involved can be fully understood. Furthermore, the thickness of the coating is a parameter that heavily influences the resulting spectra, however in this study it wasn't controlled. Still, these preliminary results show that the interrogation unit developed is able to interrogate sensors with low sensitivity and detect short wavelength shifts.

Chapter 6

Final Remarks and Future Work

A compact interrogation unit capable of sensing optical fiber sensors in the near infrared region was designed and built with a total cost lower than 300 euro. The results are comparable to those obtained with commercial OSAs when interrogating LPFGs in different conditions at much lower cost. However it should be noted that the unit can be used for the interrogation of most optical fiber based sensors in the working range of 1350 to 1650nm, namely FBGs and plasmonic bands should be considered in future work.

Most of the measurements shown were taken using a C and L band light source, which is fairly expensive and limited to a short region of the working range. However, due to the optimization of light using the GRIN lens, the precision amplifier circuit and deconvolution, the use of much cheaper broadband Halogen-Tungsten white-light sources was shown to be a possibility, despite the low coupling efficiency to the fiber.

The application of the deconvolution technique allowed for a more accurate estimation of the real input signal, however the results were very dependent on the estimation of the impulse response and the noise-desensitising factor used. Very preliminary results show that total variation regularization can help stabilize the deconvolution with the noise-desensitising parameter, even for signals with low signal-to-noise ratio but a more thorough study must be performed. Other deconvolution methods can also be studied in the future, such as iterative techniques and other figures of merit should be considered to compare the signals before and after deconvolution.

The use of multiple MEMS-FPI spectrum sensors can also be considered as it would allow for the multiplexing of different sensors and, depending on their characteristics, allow for the expansion of the working range of the interrogation unit.

Appendix A

Matrix Method for Cladding Mode Refractive Indexes.

For the core mode the matrix described in 2.10 can be written as:

$$\begin{pmatrix} ik_0E^{(z)} \\ -k_0H^{(z)} \\ iE^{(\varphi)} \\ H^{(\varphi)} \end{pmatrix} = \begin{pmatrix} -\frac{u_1^2}{\varepsilon_1}J_v(u_1r) & 0 & 0 & 0 \\ 0 & 0 & u_1^2J_v(u_1r) & 0 \\ \frac{\sigma}{r\varepsilon_1}J_v(u_1r) & 0 & -u_1J_v^{'}(u_1r) & 0 \\ -u_1J_v^{'}(u_1r) & 0 & \frac{\sigma}{r}J_v(u_1r) & 0 \end{pmatrix} \begin{pmatrix} A_1 \\ 0 \\ C_1 \\ 0 \end{pmatrix} \tag{A.1}$$

A similar matrix can be written for the cladding (layer 2):

$$M_2 = \begin{pmatrix} -\frac{u_2^2}{\varepsilon_2}J_v(u_2r) & -\frac{u_2^2}{\varepsilon_2}Y_v(u_2r) & 0 & 0 \\ 0 & 0 & u_2^2J_v(u_2r) & u_2^2Y_v(u_2r) \\ \frac{\sigma}{r\varepsilon_2}J_v(u_2r) & \frac{\sigma}{r\varepsilon_2}Y_v(u_2r) & -u_2J_v^{'}(u_2r) & -u_2Y_v^{'}(u_2r) \\ -u_2J_v^{'}(u_2r) & -u_2Y_v^{'}(u_2r) & \frac{\sigma}{r}J_v(u_2r) & \frac{\sigma}{r}Y_v(u_2r) \end{pmatrix} \tag{A.2}$$

Where the fields follow the expression:

$$\begin{pmatrix} ik_0E^{(z)} \\ -k_0H^{(z)} \\ iE^{(\varphi)} \\ H^{(\varphi)} \end{pmatrix} = M_2 \begin{pmatrix} A_2 \\ B_2 \\ C_2 \\ D_2 \end{pmatrix} \tag{A.3}$$

Finally, because the field decays outside the fiber, it can be expected that $k_0^2\varepsilon_3 - \beta^2$ is negative. This means that the parameters A_3 and C_3 are equal to zero. So, for the external layer we can write:

$$M_3 = \begin{pmatrix} 0 & \frac{w_3^2}{\varepsilon_3} K_v(w_3 r) & 0 & 0 \\ 0 & 0 & 0 & -w_3^2 K_v(w_3 r) \\ 0 & \frac{\sigma}{r\varepsilon_3} K_v(w_3 r) & 0 & -w_3 K_v^{'}(w_3 r) \\ 0 & -w_3 K_v^{'}(w_3 r) & 0 & \frac{\sigma}{r} K_v(w_3 r) \end{pmatrix} \tag{A.4}$$

where $w_3 = \sqrt{\beta^2 - k_0^2 \varepsilon_3}$.

The boundary conditions can be expressed in the matrix form as:

$$M_1(a_1) \begin{pmatrix} A_1 \\ 0 \\ C_1 \\ 0 \end{pmatrix} = M \begin{pmatrix} 0 \\ B_3 \\ 0 \\ D_3 \end{pmatrix}, \tag{A.5}$$

where $M = M_2(a_1) M_2^{-1}(a_2) M_3(a_2)$. Using the elements of matrices M and M_1 we can write matrix N such that:

$$N = \begin{pmatrix} -m_{11}^{(1)} & m_{12} & -m_{13}^{(1)} & m_{14} \\ -m_{21}^{(1)} & m_{22} & -m_{23}^{(1)} & m_{24} \\ -m_{31}^{(1)} & m_{32} & -m_{33}^{(1)} & m_{34} \\ -m_{41}^{(1)} & m_{42} & -m_{43}^{(1)} & m_{44} \end{pmatrix} \tag{A.6}$$

where m_{ij} and $m_{ij}^{(1)}$ correspond to the elements of matrices M and M_1, respectively. With this, equation A.5 can be rewritten as:

$$N \begin{pmatrix} A_1 \\ B_3 \\ C_1 \\ D_3 \end{pmatrix} = 0 \tag{A.7}$$

By setting the determinant of matrix N to zero, an equation with the single unknown variable β is obtained. The solutions of $det(N) = 0$ are the set of propagation constants for the various cladding modes. With this it is possible to obtain their respective effective indexes.

Appendix B

Other Figures

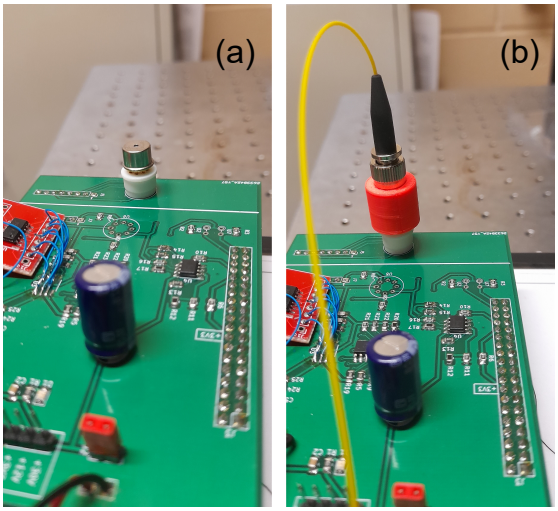

FIGURE B.1: MEMS-FPI Spectrum Sensor in the Printed Circuit Board: (a) shows a photograph of the sensor set up and (b) shows the the FC-PC connector held in place by the designed 3D printed piece.

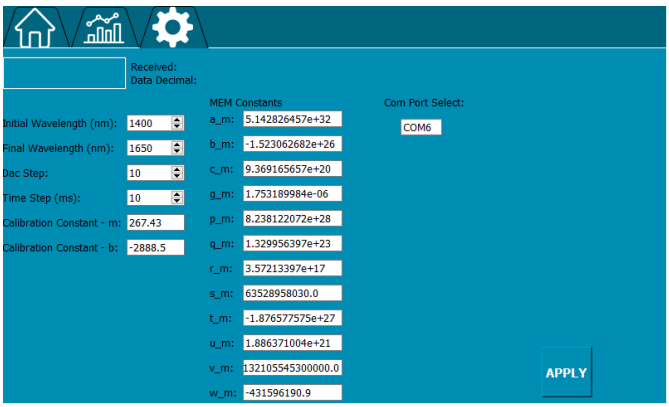

FIGURE B.2: Graphical interface configuration window.

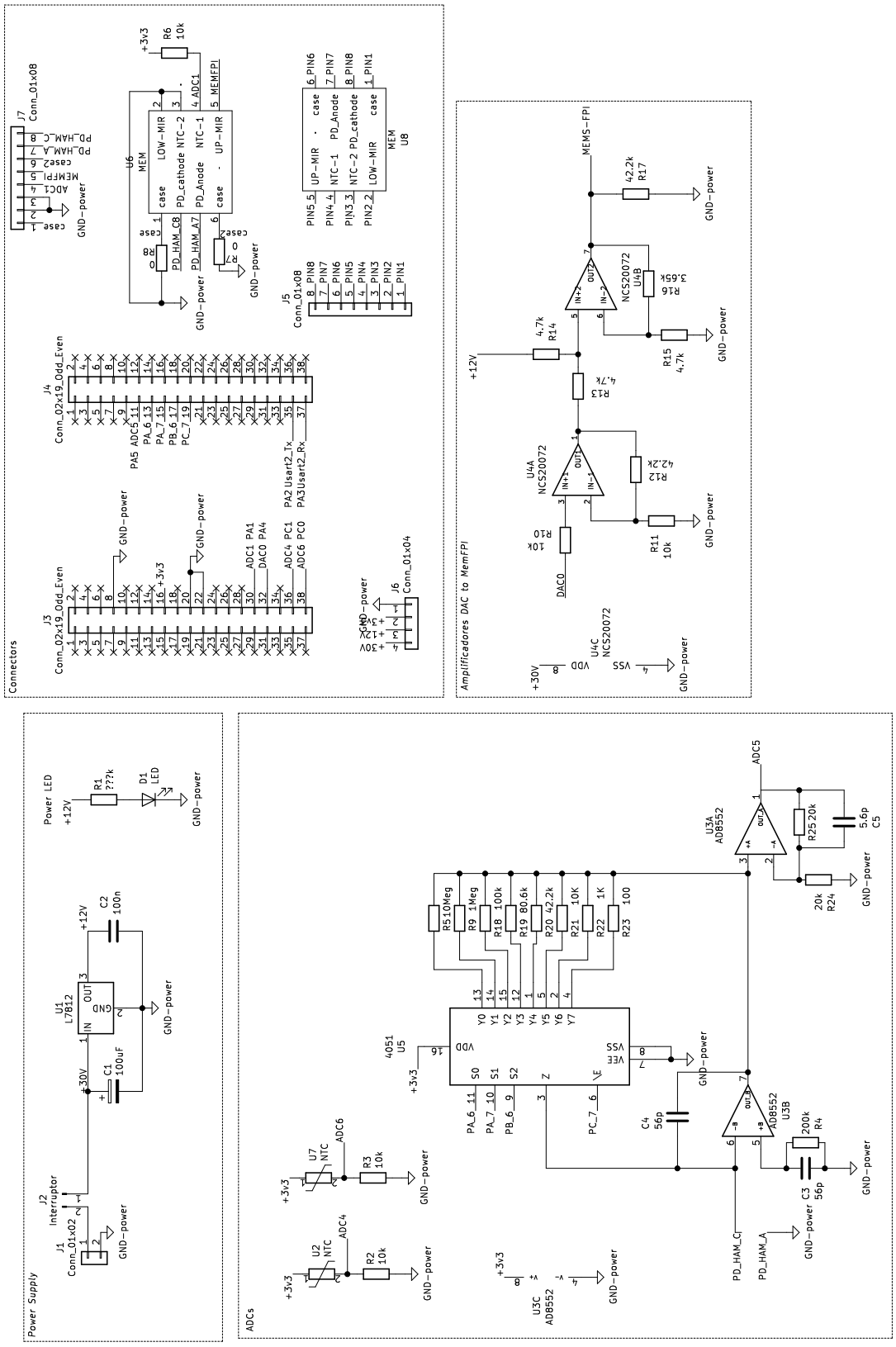

FIGURE B.3: Full Printed Circuit Board Schematic.

Bibliography

[1] J. Chen, B. Liu, and H. Zhang, "Review of fiber bragg grating sensor technology," *Frontiers of Optoelectronics in China*, vol. 4, no. 2, pp. 204–212, 2011. [Cited on page 3.]

[2] K. O. Hill, Y. Fujii, D. C. Johnson, and B. S. Kawasaki, "Photosensitivity in optical fiber waveguides: Application to reflection filter fabrication," *Applied Physics Letters*, vol. 32, no. 10, p. 647, May 1978. [Cited on page 3.]

[3] A. M. Vengsarkar, P. J. Lemaire, J. Judkins, V. Bhatia, T. Erdogan, and J. E. Sipe, "Long-period fiber gratings as band-rejection filters," *Journal of Lightwave Technology*, vol. 14, pp. 58–65, 1996. [Cited on page 3.]

[4] S. W. James and R. P. Tatam, "Optical fibre long-period grating sensors: characteristics and application," *Measurement Science and Technology*, vol. 14, no. 5, pp. R49–R61, mar 2003. [Online]. Available: https://doi.org/10.1088/0957-0233/14/5/201 [Cited on pages 3, 6, and 8.]

[5] S.-Y. Tan, Y.-T. Yong, S.-C. Lee, and F. A. Rahman, "Review on an arc-induced long-period fiber grating and its sensor applications," *Journal of Electromagnetic Waves and Applications*, vol. 29, no. 6, pp. 703–726, 2015. [Online]. Available: https://doi.org/10.1080/09205071.2015.1021019 [Cited on page 3.]

[6] C. Wang, Y. Zhang, J. Sun, C. Yang, X. Ren, J. Li, and D. Zhang, "Research on a fiber bragg grating temperature measurement method for inter-satellite laser link," *Review of Scientific Instruments*, vol. 91, no. 1, p. 015007, 2020. [Cited on page 4.]

[7] T. Erdogan, "Cladding-mode resonances in short- and long-period fiber grating filters," *J. Opt. Soc. Am. A*, vol. 14, no. 8, pp. 1760–1773, Aug 1997. [Online]. Available: http://opg.optica.org/josaa/abstract.cfm?URI=josaa-14-8-1760 [Cited on pages 4 and 11.]

[8] Erdogan, "Fiber grating spectra," *Journal of Lightwave Technology*, vol. 15, no. 8, pp. 1277–1294, 1997. [Cited on pages 4 and 5.]

[9] S.-Y. Tan, Y.-T. Yong, S.-C. Lee, and F. Abd-Rahman, "Review on an arc-induced long-period fiber grating and its sensor applications," *Journal of Electromagnetic Waves and Applications*, vol. 29, 03 2015. [Cited on pages 4 and 7.]

[10] R. Y. Wong, E. Chehura, S. E. Staines, S. W. James, and R. P. Tatam, "Fabrication of fiber optic long period gratings operating at the phase matching turning point using an ultraviolet laser," *Applied Optics*, vol. 53, no. 21, pp. 4669–4674, 2014. [Cited on pages 6 and 7.]

[11] B. J. O'Regan and D. N. Nikogosyan, "Femtosecond uv long-period fibre grating fabrication with amplitude mask technique," *Optics Communications*, vol. 284, no. 24, pp. 5650–5654, 2011. [Online]. Available: https://www.sciencedirect.com/science/article/pii/S003040181100887X [Cited on pages 6 and 7.]

[12] A. Martinez-Rios, D. Monzon-Hernandez, I. Torres, and G. Salceda-Delgado, *Long Period Fibre Gratings*. IntechOpen, 02 2012. [Cited on page 6.]

[13] C. Poole, H. Presby, and J. Meester, "Two-mode fibre spatial-mode converter using periodic core deformation," *Electronics Letters*, vol. 30, no. 17, pp. 1437–1438, 1994. [Cited on page 7.]

[14] G. Rego, "Arc-induced long period fiber gratings," *journal of Sensors*, vol. 2016, 2016. [Cited on page 7.]

[15] ——, "Annealing of arc-induced gratings at high temperatures," *Electronics letters*, vol. 45, no. 19, pp. 972–974, 2009. [Cited on page 7.]

[16] Y. Kondo, K. Nouchi, T. Mitsuyu, M. Watanabe, P. G. Kazansky, and K. Hirao, "Fabrication of long-period fiber gratings by focused irradiation of infrared femtosecond laser pulses," *Optics letters*, vol. 24, no. 10, pp. 646–648, 1999. [Cited on page 8.]

[17] T. Allsop, K. Kalli, K. Zhou, G. Smith, M. Komodromos, K. Sugden, M. Dubov, D. J. Webb, and I. Bennion, "Comparison between femtosecond laser and fusion-arc inscribed long period gratings in photonic crystal fibre," in *Photonic Crystal Fibers III*, vol. 7357. SPIE, 2009, pp. 149–158. [Cited on page 8.]

[18] B. Li, L. Jiang, S. Wang, H.-L. Tsai, and H. Xiao, "Femtosecond laser fabrication of long period fiber gratings and applications in refractive index sensing," *Optics & Laser Technology*, vol. 43, no. 8, pp. 1420–1423, 2011. [Online]. Available: https://www.sciencedirect.com/science/article/pii/S0030399211000983 [Cited on page 8.]

[19] T. Wei, J. Montoya, J. Zhang, J. Dong, and H. Xiao, "Fabrication of long-period fiber gratings by co2 laser irradiations for high temperature applications," in *Sensors for Harsh Environments III*, vol. 6757. SPIE, 2007, pp. 44–48. [Cited on page 8.]

[20] L. Drozin, P. Fonjallaz, and L. Stensland, "Long-period fibre gratings written by coˆ sub 2ˆ exposure of hˆ sub 2ˆ-loaded, standard fibres," *Electronics Letters*, vol. 36, no. 8, p. 1, 2000. [Cited on page 8.]

[21] C.-H. Lin, Q. Li, A. A. Au, Y. Jiang, E. Wu, and H. P. Lee, "Strain-induced thermally tuned long-period fiber gratings fabricated on a periodically corrugated substrate," *Journal of lightwave technology*, vol. 22, no. 7, p. 1818, 2004. [Cited on page 8.]

[22] C.-Y. Lin, G.-W. Chern, and L. A. Wang, "Periodical corrugated structure for forming sampled fiber bragg grating and long-period fiber grating with tunable coupling strength," *Journal of Lightwave Technology*, vol. 19, no. 8, p. 1212, 2001. [Cited on page 8.]

[23] P. Caldas, "Fiber optic sensing by evanescent field interaction," *Ph.D. dissertation*, 2011. [Cited on page 10.]

[24] C. R. Doerr and H. Kogelnik, "Dielectric waveguide theory," *Journal of Lightwave Technology*, vol. 26, no. 9, pp. 1176–1187, 2008. [Cited on page 10.]

[25] ofiber documentation. Accessed: 2022. [Online]. Available: https://ofiber.readthedocs.io/en/latest/ [Cited on page 10.]

[26] C. Tsao, *Optical fibre waveguide analysis*. Oxford University Press, 1992. [Cited on page 11.]

[27] O. Ivanov, S. Nikitov, and Y. Gulyaev, "Cladding modes of optical fibers: Properties and applications," *Physics-Uspekhi*, vol. 49, p. 167, 02 2006. [Cited on pages 11 and 12.]

[28] S.-Y. Tan, Y.-T. Yong, S.-C. Lee, and F. Abd Rahman, "Review on an arc-induced long-period fiber grating and its sensor applications," *Journal of Electromagnetic Waves and Applications*, vol. 29, no. 6, pp. 703–726, 2015. [Cited on pages 11 and 12.]

[29] L. Coelho, D. Viegas, J. L. Santos, and J. De Almeida, "Enhanced refractive index sensing characteristics of optical fibre long period grating coated with titanium dioxide thin films," *Sensors and Actuators B: Chemical*, vol. 202, pp. 929–934, 2014. [Cited on page 13.]

[30] J. K. Sahota, N. Gupta, and D. Dhawan, "Fiber bragg grating sensors for monitoring of physical parameters: A comprehensive review," *Optical Engineering*, vol. 59, no. 6, p. 060901, 2020. [Cited on page 14.]

[31] P. S. dos Santos, P. A. Jorge, J. M. de Almeida, and L. Coelho, "Low-cost interrogation system for long-period fiber gratings applied to remote sensing," *Sensors*, vol. 19, no. 7, p. 1500, 2019. [Cited on page 14.]

[32] J. Carvalho, L. Coelho, M. Pontes, A. Barbero, M. Martinez, R. Ribeiro, J. Weyl, J. Baptista, M. Giraldi, I. Dias *et al.*, "Long-period gratings dynamic interrogation with modulated fiber bragg gratings and optical amplification," *IEEE Sensors Journal*, vol. 12, no. 1, pp. 179–183, 2011. [Cited on page 14.]

[33] M. Ebermann, N. Neumann, K. Hiller, M. Seifert, M. Meinig, and S. Kurth, "Tunable MEMS Fabry-Pérot filters for infrared microspectrometers: a review," in *MOEMS and Miniaturized Systems XV*, W. Piyawattanametha and Y.-H. Park, Eds., vol. 9760, International Society for Optics and Photonics. SPIE, 2016, pp. 64 – 83. [Online]. Available: https://doi.org/10.1117/12.2209288 [Cited on pages 14 and 16.]

[34] Mems-fpi c14272 spectrum sensor datasheet - hamamatsu. Accessed: 2022. [Online]. Available: https://www.hamamatsu.com/content/dam/hamamatsu-photonics/sites/documents/99_SALES_LIBRARY/ssd/c14272_kacc1259e.pdf [Cited on pages 15, 16, 18, and 37.]

[35] Mems-fpi c13272-03 spectrum sensor datasheet - hamamatsu. Accessed: 2022. [Online]. Available: https://www.hamamatsu.com/content/dam/hamamatsu-photonics/sites/documents/99_SALES_LIBRARY/ssd/c13272-03_kacc1295e.pdf [Cited on page 15.]

[36] Mems-fpi c14273 spectrum sensor datasheet - hamamatsu. Accessed: 2022. [Online]. Available: https://www.hamamatsu.com/content/dam/hamamatsu-photonics/sites/documents/99_SALES_LIBRARY/ssd/c14273_kacc1265e.pdf [Cited on page 15.]

[37] N. Neumann, M. Ebermann, S. Kurth, and K. Hiller, "Tunable infrared detector with integrated micromachined fabry-perot filter," *Journal of Micro/Nanolithography, MEMS, and MOEMS*, vol. 7, no. 2, p. 021004, 2008. [Cited on page 17.]

[38] F. Honarvar, H. Sheikhzadeh, M. Moles, and A. N. Sinclair, "Improving the time-resolution and signal-to-noise ratio of ultrasonic nde signals," *Ultrasonics*, vol. 41, no. 9, pp. 755–763, 2004. [Cited on pages 18 and 19.]

[39] E. O. Brigham and R. Morrow, "The fast fourier transform," *IEEE spectrum*, vol. 4, no. 12, pp. 63–70, 1967. [Cited on page 19.]

[40] T. Wang, Ö. Özdamar, J. Bohórquez, Q. Shen, and M. Cheour, "Wiener filter deconvolution of overlapping evoked potentials," *Journal of neuroscience methods*, vol. 158, no. 2, pp. 260–270, 2006. [Cited on page 19.]

[41] H.-J. Van Manen, R. Bloemenkamp, and O. F. Van Den Brink, "Focal length determination of raman immersion ball probes in diverse media," *Applied spectroscopy*, vol. 63, no. 3, pp. 378–380, 2009. [Cited on page 20.]

[42] Winlens3d basic. Accessed: 2022. [Online]. Available: https://www.opticalsoftware.net/index.php/how_to/lens_design_software/winlens3d [Cited on page 20.]

[43] D. Savastru, M. Popescu, S. Miclos, F. Sava, A. Lorinczi, M. Rusu, and V. Savu, "Single mode optical fiber coupling to a laser diode," *Optical Memory and Neural Networks*, vol. 17, no. 4, pp. 254–257, 2008. [Cited on page 21.]

[44] Gofoton single fiber collimator. Accessed: 2022. [Online]. Available: https://www.gofoton.co.jp/userimage/pdf/1/Single-Fiber-Collimators-gf.pdf [Cited on page 22.]

[45] Stm32f091rc nucleo board. Accessed: 2022. [Online]. Available: https://www.st.com/resource/en/datasheet/stm32f091rc.pdf [Cited on pages 25 and 27.]

[46] Kicad, open source electronics design. Accessed: 2022. [Online]. Available: https://www.kicad.org/ [Cited on page 27.]

[47] Pyqt5 documentation. Accessed: 2022. [Online]. Available: https://www.riverbankcomputing.com/static/Docs/PyQt5 [Cited on page 32.]

[48] B. Dias, J. Carvalho, J. P. Mendes, J. M. Almeida, and L. C. Coelho, "Analysis of the relative humidity response of hydrophilic polymers for optical fiber sensing," *Polymers*, vol. 14, no. 3, p. 439, 2022. [Cited on page 41.]